MoTe₂ Lateral Homojunction Field-Effect Transistors Fabricated using Flux-Controlled Phase Engineering

Rui Ma,¹ Huairuo Zhang,²,³* Youngdong Yoo,⁴ Zachary Patrick Degregorio,⁵ Lun Jin,⁵ Prafful Golani,¹ Javad Ghasemi Azadani,¹ Tony Low,¹ James E. Johns,⁵ Leonid A. Bendersky,³ Albert V. Davydov,³ and Steven J. Koester¹*

¹Dept. of Electrical & Computer Engineering, University of Minnesota, Minneapolis, MN 55455, USA

²Theiss Research, Inc., La Jolla, California 92037, USA

³Materials Science and Engineering Division, National Institute of Standards and Technology (NIST), Gaithersburg, MD 20899, USA

⁴Department of Chemistry, Ajou University, Suwon 16499, Korea

⁵Department of Chemistry, University of Minnesota, Minneapolis, MN 55455, USA

*Corresponding Authors: skoester@umn.edu (S.J.K.); huairuo.zhang@nist.gov (H.Z.)

ABSTRACT

The coexistence of metallic and semiconducting polymorphs in transition metal dichalcogenides (TMDCs) can be utilized to solve the large contact resistance issue in TMDC-based field effect transistors (FETs). Semiconducting hexagonal (2H) molybdenum ditelluride (MoTe₂) phase, metallic monoclinic (1T') MoTe₂ phase and their lateral homojunctions can be selectively synthesized in situ by chemical vapor deposition due to the small free energy difference between the two phases. Here, we have investigated, in detail, the structural and electrical properties of in-situ-grown lateral 2H/1T' MoTe₂ homojunctions grown using flux-controlled phase engineering. Using atomic-resolution plan-view and cross-sectional transmission electron microscopy analyses, we show that the round regions of near-single-crystalline 2H-MoTe₂ grow out of a polycrystalline 1T'-MoTe₂ matrix. We further demonstrate the operation of MoTe₂ FETs made on these in-situ-grown lateral homojunctions with 1T' contacts. The use of 1T' phase as electrodes in MoTe₂ FETs effectively improves device performance by substantially decreasing the contact resistance. The contact resistance of 1T' electrodes extracted from the transfer length method measurements is $470 \pm 30 \Omega$ -µm. Temperature- and gate-voltage-dependent transport characteristics reveal a flat-band barrier height of ~ 30 + 10 meV at the lateral 2H/1T' interface that is several times smaller, and shows stronger gate modulation, compared to the metal-2H Schottky barrier height. The information learned from this analysis will be critical to understanding the properties of MoTe₂ homojunction FETs for use in memory and logic circuity applications.

KEYWORDS: transition metal dichalcogenide, Schottky barrier height, chemical vapor deposition, phase engineering, MoTe₂, lateral homojunction

Transition metal dichalcogenides (TMDCs) have been widely studied for electronic applications, such as integrated circuits¹⁻⁴ and memory devices, ^{1,2,5-9} due to their layered crystal structures and polymorphism with distinct electronic properties. TMDCs in their semiconducting polymorph typically have tunable band gaps (1-2 eV) making them well-suited for use in CMOS logic circuits. Although field-effect transistors (FETs) based on two-dimensional TMDCs exhibit high current on/off ratio, ¹⁰⁻¹³ small subthreshold swing,^{4, 14} and low leakage current,⁵ the relatively high contact resistance at the metal/TMDCs interface remains a challenging issue that limits their performance. ¹⁵⁻²⁰ Strategies that have proven effective in reducing the contact resistance include optimizing the contact metals, ²¹ chemical doping, ^{22,23} plasma treatment, ²⁴ and sandwiching graphene²⁵⁻²⁷ as an intermediate contact material.

Structural polymorphic phase transition from the semiconducting phase to the metallic phase in TMDCs is a promising way to achieve low-resistance contacts in TMDCs-based FETs. Theoretically, for all Mo- and W-based TMDCs, their hexagonal (2H) phase is semiconducting while tetragonal (1T)/monoclinic (1T') phase is metallic/semi-metallic. ²⁸, ²⁹ The contact resistance can be dramatically reduced by converting the 2H phase to the 1T or 1T' phase in the contact regions of TMDCs-based FETs. Among all the 2H Mo- or W-based compounds, molybdenum ditelluride (MoTe₂) requires the least amount of energy (35 meV per MoTe₂ formula unit) to convert coherently from 2H to 1T'. ³⁰⁻³² Due to the small energy difference, this 2H to 1T' conversion has been achieved by electrostatic doping, ³³ laser irradiation, ³⁴ the use of tensile strain, ³⁵ etc. All those phase transitions were observed in exfoliated 2H-MoTe₂ and only the report in reference 34 demonstrated heterostructure FETs using the phase-transitioned 1T' MoTe₂ in the contact regions. On the other hand, several reports ³⁶⁻⁴⁰ have described *in-situ*-grown MoTe₂ homojunctions produced by various means including tellurization-velocity-

dependent phase evolution,^{36,37} post-growth annealing to induce a 2H to 1T' phase transition,³⁸ temperature-selective phase stabilization in the presence of NaCl,³⁹ and flux-controlled phase engineering.⁴⁰

The flux-controlled phase engineered growth technique for 2H/1T' heterojunctions is of particular interest given its robustness and ability to form large grains. ⁴¹ In this technique, the phase of MoTe₂, can be controlled during growth simply by exposing elemental Mo to differing amounts of Te atomic flux. In our previous work, multi-layer lateral MoTe₂ homojunctions have been successfully synthesized on SiO₂/Si substrates using this technique. ⁴⁰ The fact that the phases form *via* a solid-to-solid phase transition ⁴¹ makes understanding these interfaces important for FETs as well as phase-change-based memristive devices. ⁴², ⁴³ However, a comprehensive study combining detailed microstructural and electrical properties of 2H/1T' MoTe₂ interfaces formed *via* the flux-controlled growth technique has not been reported.

In this work, we characterize the microstructural properties of flux-controlled, *in-situ*-grown lateral 2H/1T' MoTe₂ homojunctions by using atomic-resolution transmission electron microscopy (TEM) for both plan-view and cross-sectional samples. We demonstrate improved performance of the homojunction FETs compared to 2H-only devices with metal/2H contacts, and report record-low contact-resistance in FETs that incorporate these lateral 2H/1T' MoTe₂ homojunctions. Furthermore, we evaluate the energy barrier at the 2H/1T' interface as a function of applied gate voltage by performing temperature-dependent transport measurements and find a substantially lower energy barrier compared to direct metal contacts to 2H-MoTe₂ over the entire gate biasing window. Density functional theory (DFT) calculations are also performed to estimate the expected band line ups at the 2H/1T' interface.

RESULTS AND DISCUSSION

The material synthesis started by using n-Si substrates upon which 300 nm of SiO₂ was grown by thermal oxidation. MoTe₂ was then grown on the wafers by first depositing a nanolayer of Mo followed by reacting the Mo with Te at controlled rates at 585 °C for 60 min. Under these conditions, MoTe₂ forms with a mixture of 2H and 1T' phases, as described in our previous work. 40 With this growth technique the thickness of the films can vary by a few nm due to variations in growth conditions and the thickness of the initial deposited Mo. The AFM height map of a grown MoTe₂ homojunction in Figure S1 of the Supporting Information shows a thickness of 8 nm and no systematic change in height across the 2H/1T' interface. By optimizing the growth conditions, our CVD method is capable of growing homojunction films with a thickness of down to 3.5 nm (5-layer). 40 Next, mesa regions were patterned and etched into the MoTe₂ to form rectangular areas consisting of 2H, 1T' and 2H/1T' nanosheets. Contacts to the MoTe₂ were formed by patterning and lifting off Ti (10 nm) / Au (80 nm) contacts. Details of the MoTe₂ synthesis and device fabrication are provided in the Methods section. Three types of devices were fabricated: (1) 2H-only devices where the channel consisted of 2H phase and the metal pads were contacted to the 2H phase, (2) 1T'-only devices where the channel consisted of 1T' phase and the metal pads were contacted to the 1T' phase, and (3) 2H/1T' devices where the channel consisted of 2H phase and the metal pads were contacted to the 1T' phase. A schematic diagram of a lateral monolayer 2H/1T' MoTe₂ nanosheet is illustrated in Figure 1a. A clear optical contrast between the 2H and 1T' MoTe₂ regions is observed from the optical image of a 2H/1T' MoTe₂ device shown in Figure 1b. Raman mapping of phase-specific phonons was used to further confirm phase identity. The Raman spectra shown in Figure 1c indicate that the center of the channel is composed of all 2H-MoTe₂ and the edges adjacent to the contact fingers are

composed of all 1T' MoTe₂. Raman maps of the 2H-MoTe₂ E_{2g} peak (Figure 1d) and 1T' MoTe₂ B_g peak (Figure 1e) show a sharp interface between the 2H and 1T' MoTe₂ regions.

TEM was employed to gain insight into the microstructural details of the 2H/1T' MoTe₂ homojunction. Sample preparation is provided in both the Methods section and the Supporting Information (Figure S2). Figure 2a shows a low-magnification bright-field TEM image of the plan-view sample supported on lacey carbon. The round region of darker contrast is identified as having the 2H structure (see below) and the surrounding brighter matrix is identified as having the 1T' structure. Selected area electron diffraction pattern (SAEDP) analysis shows the 2H region being a near single-crystal oriented with the [001]_{2H} normal to the plane of the film (Figure 2b), and the 1T' matrix is polycrystalline but textured so that the [001]_{1T'} direction is out of the film plane (Figure 2c). Detailed analysis of the polycrystalline diffraction rings supporting the strong [001]_{1T} texture is given in Figure S3 and Table S1 of the Supporting Information. Figure 2d shows a dark-field TEM image taken with an aperture at the (100) diffraction spot shown in Figure 2b with a yellow circle. Most of the round region is bright and consistent with the SAEDP analysis of near-single-crystallinity of the 2H phase. The dark areas shown by the yellow circles have a smaller thickness than the surrounding area (Figure S4). The speckling contrast is due to the thickness variation and slight local misorientation of the 2H domains (Figure 2e, Figure S5). Figure 2f shows a dark-field image taken from the 2H/1T' interface region with a large aperture (placed as shown in the inset), evidencing the polycrystalline 1T' grains. High-resolution TEM (HRTEM) observation shows a structural continuity at the 2H/1T' interface region (Figure 2g). Figures 2h and 2i show typical HRTEM images taken from the 2H region and the 1T' matrix, respectively. The insets of projected atomic models and corresponding

simulated HRTEM images show good match with the hexagonal and orthorhombic structures of 2H and 1T' along their [001] zone-axes, respectively.

Aberration-corrected scanning TEM (STEM) was further employed to characterize the homojunction film. Figure 3a shows a low-magnification low-angle annular dark-field (LAADF) STEM image of a round 2H region surrounded by a 1T' matrix in the plan-view sample. The 2H region has stronger intensity than the 1T' matrix, apparently due to electron channeling effect along the [001]_{2H} direction. A zoomed-in LAADF-STEM image shows mottled contrast in the near-single-crystalline 2H region and nano-size polycrystalline particles in the 1T' matrix (Figure 3b), due to the thickness variations and slight local misorientations of the 2H domains and the polycrystalline 1T' matrix. Figure 3c and 3d show typical high-resolution STEM (HRSTEM) images taken from 2H and 1T' regions along the [001] zone-axis, respectively. The typical honeycomb structure of the 2H phase is identified in the entire round region and no presence of other structures such as 1T' and 3R⁴⁴ are observed. Figure 3e shows an HRSTEM image of a large area from the mottled 2H region, with the corresponding FFT image in the inset showing the single-crystallinity. The detail analysis of this image in Figure S5 shows the thickness variation and slight misorientation in local areas. Figures 3f-3h show HRSTEM images of the 2H/1T' interface region, demonstrating the 2H phase connecting seamlessly with the neighboring randomly-orientated 1T' grains. The homojunction film was further characterized with crosssectional STEM. Figure 3i shows a cross-sectional STEM image capturing both the 2H and 1T' regions. The film thickness varies between 8.5 nm and 12.9 nm along a 20-um long TEM lamellar sample. As shown by the yellow arrows in Figure 3i, the 1T' region is composed of nanosized grains which were identified as randomly textured along the [001]_{1T'} out-of-plane direction. In contrast, the film in the 2H region is continuous and very few domain boundaries

were observed; some thickness variations are shown by the purple arrows. Figures 3j-3m show some typical HRSTEM images taken from the 2H region (Figures 3j-3k) and 1T' region (Figures 3l-3m) which are well matched with the atomic models of 2H and 1T', respectively.

Next, we compare transport characteristics of all three types of devices, and extract the contact resistances at the 2H/metal and the 1T'/metal interface, and the energy barrier at the 2H/1T' interface. The contact resistances of 1T'-only and 2H-only devices were measured under vacuum using the transfer length method (TLM), as shown in Figures 4a and 4b. The contact resistance of Ti/Au to the 1T' MoTe₂ was found to be $0.47 \pm 0.03 \text{ k}\Omega$ - μ m and the sheet resistance of 1T' MoTe₂ was $2.65 \pm 0.09 \text{ k}\Omega/\Box$ at zero back-gate voltage, V_{BG} . The 1T' contact resistance value is comparable to the best value reported so far for phase-transitioned MoS₂-based FETs (200-300 Ω - μ m), ⁴⁵ and the best of our knowledge, is the lowest reported for MoTe₂. Conversely, the contact resistance of the Ti/Au metal to 2H-MoTe₂ was found to be 15.6 ± 0.58 M Ω - μ m with a sheet resistance of the 2H phase of $4.67 \pm 0.7 \text{ M}\Omega/\Box$ at $V_{BG} = -100 \text{ V}$. Thus, the contact resistance is reduced by 4 orders of magnitude by using the 1T' contacts. The back-gate dependence of the contact resistance of the 2H-only device is shown as an inset in Figure 4b. The contact resistance increases with increasing back-gate voltage as the device turns off.

The room-temperature transfer characteristics showing drain current, I_D vs. V_{BG} , of the 1T'-only and 2H-only devices are shown in Figure 4c. The 1T'-only device shows high drive current of 245 μ A/ μ m at $V_{DS} = -0.5$ V, but has no gate modulation, which confirms the metallic nature of the 1T' MoTe₂. The 2H-only device shows a typical MOSFET transfer characteristic with a current on/off ratio of ~20. The relatively small current on/off ratio can be attributed to the traps at the MoTe₂/SiO₂ interface. The calculated interface trap density in this device is on the order of

 10^{13} cm⁻²/eV at room temperature, which significantly degrades the modulation efficiency of the gate electrode. Details of the trap density extraction are provided in the Methods section. The room-temperature output characteristics (I_D vs. V_{DS}) of the 1T'-only and 2H-only devices are shown in Figure 4d. The current of the 1T'-only device is over 4 orders of magnitude larger than that of the 2H-only device at the same V_{DS} . Furthermore, the 1T'-only device has a linear relationship whereas the 2H-only device displays nonlinear behavior, which is consistent with the metallic (semiconducting) nature of the 1T' MoTe₂ (2H-MoTe₂) material.

Figure 5 shows the temperature-dependent device behavior for the 2H-only and 2H/1T' device geometries depicted schematically in Figures 5a and 5b, The I_D vs. V_{BG} characteristics of these devices are shown in Figures 5c and 5d, respectively, for temperatures ranging from 77 K to 300 K (optical images of these devices are inset in Figures 5e and 5d). As expected, the oncurrent, current on/off ratio and subthreshold swing, SS, are improved by using 1T' electrodes. For the 2H/1T' device, the current on/off ratio increases and SS reduces with decreasing temperature, strongly suggesting that the current of the 2H/1T' device is in the mobility-limited, as opposed to the thermionic-limited regime. This improvement of the current on/off ratio is not prominent in the 2H-only device, showing that the current is limited by thermionic transport associated with the metal/2H-MoTe₂ interface. Table 1 provides a performance comparison of the 2H-only and 2H/1T' devices. Once again, the relatively low on-current in our devices is consistent with the presence of interface traps, which can occur despite the high crystal quality of the 2H-MoTe₂ itself. The field-effect hole mobility of the 2H/1T' device (7.4 cm²/Vs) is \sim 10 times higher than that of the 2H-only device (0.8 cm²/Vs) and shows a dependence on temperature with a power factor of 1.5, confirming the Ohmic contact at the metal/1T' interface. Accounting for the effect of interface traps in our samples, these mobility values are comparable

with previously reported values for CVD-grown MoTe₂.^{36,39,46} Additional details of the field-effect hole mobility extraction and its temperature dependency are provided in the Supporting Information (Figure S6).

The improvement in the contact resistance using the metal/1T' electrode design is also observed in the output characteristics (I_D vs. V_{DS}) of the devices as shown in Figures 5e and 5f. The linear output characteristics of the 2H/1T' device at 300 K and 77 K indicates Ohmic-like behavior of the 1T' electrode and the 2H/1T' interface, whereas the output characteristics of the 2H device is nonlinear and becomes severe at lower temperature implying the presence of a Schottky behavior at the metal/2H interface. Furthermore, the on-state drain current values (at $V_{BG} = -100 \text{ V}$) in the 2H/1T' device increases with decreasing temperature, whereas the drive current decreases in the 2H-only device with decreasing temperature, suggesting mobility-limited transport in the 2H/1T' device and thermionic-limited transport in the 2H-only device. The temperature-dependent transport characteristics (Figure S7) of another set of 2H-only and 2H/1T' devices show nearly identical trends suggesting the generality of the observed results. Histograms (Figure S8) of normalized on-state resistances for three types of devices fabricated on films from four different growths with slightly different thicknesses (99 devices in total, listed in Table S2) further confirm the reproducibility of the observed trends.

Results of the temperature-dependent transfer characteristics were used to extract the Schottky barrier heights for the three interfaces: (1) metal/2H phase, (2) metal/1T', and (3) $^{2H/1T'}$. The thermionic emission equation was utilized to model the temperature and bias dependence of the drain current, I_D , as shown below (where typical units are given for the relevant parameters):

$$I_D = A^{**} T^{1.5} \exp \left[-\frac{1}{k_B T} \left(\Phi_{SB} - \frac{q V_{DS}}{\eta} \right) \right],$$
 (1)

where A^{**} is the effective Richardson constant (A/K^{1.5}), T is the temperature (K), $k_{\rm B}$ is Boltzmann's constant (eV/K), $\Phi_{\rm SB}$ is the effective Schottky barrier height for holes (eV), and $qV_{\rm DS}$ is the product of the electronic charge and drain-to-source voltage (eV), and η is the ideality factor. The term $(\Phi_{\rm SB} - qV_{\rm DS}/\eta)$ is the activation energy. $\Phi_{\rm SB}$ at each gate voltage is extracted using an Arrhenius plot, where $\ln(I_{\rm D}/T^{1.5})$ is plotted vs. $1/k_{\rm B}T$, at different values of $V_{\rm DS}$.

The Arrhenius plots for a 1T'-only device at $V_{\rm BG} = 0$ V for temperature ranging from 160 K to 260 K are shown in Figure 6a. The slopes of the Arrhenius plots are found to be positive, which indicates a negative activation energy. Negative activation energy suggests that the conductivity of the 1T' MoTe₂ decreases with increasing temperature, which implies that the 1T' MoTe₂ has metallic-like conductivity. Figure 6b shows the Arrhenius plots for a 2H-only device at $V_{\rm BG} = 0$ V for temperatures ranging from 220 K to 300 K. Here, a negative slope was found, indicating activated transport, and similar behavior was found for all values of $V_{\rm BG}$ measured in this study for the 2H-only device. Finally, Figure 6c shows the Arrhenius plot for the 2H/1T' device at $V_{\rm BG} = 0$ V for temperatures between 240 K and 300 K. Once again, a negative slope is observed, indicating thermally activated transport, though the slope is lower than that of the 2H-only device, indicating a lower energy barrier. However, as described above, since no thermally-activated transport was observed for the metal/1T' interface, we conclude that the energy barrier associated with transport in the 2H/1T' device is associated with the 2H/1T' interface and not the metal/1T' interface.

We performed analysis of the activation behavior of the carrier transport by investigating the dependence upon the backgate voltage, V_{BG} , at a fixed V_{DS} . The results are shown in Figures 7a and 7b for the 2H-only and 2H/1T' devices, respectively, where the Arrhenius plots are shown for five different values of V_{BG} . For the 2H-only device, thermally activated transport was observed for all values of V_{BG} , as indicated by the negative slope, where the slope was found to increase with more positive V_{BG} , with only slight deviation of the slope at lower temperatures. However, the 2H/1T' devices display very different behavior, with two distinct activation energies regimes, one at high temperature and another at low temperatures. First, in the high temperature regime (between 240 K and 300 K) we observe a positive slope at the most negative values of V_{BG} , indicating more metallic-like transport in the strong accumulation region. As V_{BG} increased, the slope was found to change signs and then sharply steepen as V_{BG} was made more positive. In the low temperature regime (between 100 K and 160 K), a negative slope is observed under all conditions, which only changes slightly as V_{BG} is changed.

In order to determine the complete dependence of Φ_{SB} on V_{BG} for both devices, the effect of V_{DS} on the activation energy must be taken into account. To do this, the slopes from the Arrhenius curves at a particular value of V_{BG} can be plotted vs. V_{DS} and then extrapolated to $V_{DS} = 0$. An example of this extrapolation is shown in the Supporting Information (Figure S9). This procedure was followed for all devices in order to determine Φ_{SB} as a function of V_{BG} . The results are shown in Figure 7c for both the 2H-only device in the high-temperature regime (red squares) and the 2H/1T' device in the high- and low-temperature regimes (close and open blue circles, respectively). Similar results are observed in other devices from the same substrate (Figure S10).

Several interesting trends are observable from Figure 7c. First, the overall barrier height for the 2H/1T' device in the high-temperature regime is dramatically lower than that of the 2H-only device over all V_{BG} values. Given that no thermally-activated barrier exists at the metal/1T' interface, this result indicates that the 2H/1T' valence band energy barrier is smaller than the metal/2H energy barrier, in the case of Ti as the Schottky metal. The effective barrier heights at zero backgate voltage for several 2H-only or 2H/1T' devices with different channel thicknesses have a high level of agreement (Figure S11). The flat-band barrier height at the 2H/1T' interface is estimated to be roughly 30 ± 10 meV as illustrated in Figure S12. The metal/2H barrier is qualitatively consistent with the effective Schottky barrier heights extracted for metal contacts to exfoliated 2H-MoTe₂, 23,47,48 and the 2H/1T' energy barrier is also consistent with that observed for exfoliated MoTe₂ with process-induced 1T' regions, 34 and NaCl-phase-stabilized direct epitaxy, 39

A second feature we observe is that the gate voltage dependence of the barrier height (in the high-temperature regime) is much weaker for the 2H-only device compared to the 2H/1T' device. We believe the relatively soft barrier height dependence *vs.* gate voltage for the 2H-only device is due to a combination of two factors. The first is the presence of interface traps at the MoTe₂/SiO₂ boundary that results from the CVD growth procedure. Secondly, it is well known that direct metal contacts to 2D semiconductors can have a relatively long transfer length, where the majority of current is injected underneath the contacts, as opposed to at the contact edge. 49-52 In our devices, this is confirmed by our data in Figure 4b, which shows a transfer length of several microns. In this situation, the termination of the gate-voltage induced electric field on the metal contacts further reduces the efficiency of the gate modulation. It is the combination of these two effects that leads to very little barrier height modulation. Comparison of band diagrams

at the metal/2H and 2H/1T' interfaces under different backgate voltages illustrates the effect of the longer transfer length in the 2H-only device (Figure S13), in agreement with previous reports.³⁹ It should be noted that, in the literature, the effective barrier height for metal contacts to exfoliated 2H-MoTe₂ has been found to have a strong gate voltage dependence, with the barrier height increasing to 300 meV near the transistor off-state to near zero in the strong on-state region.⁴⁷ However, in those devices larger gate modulation is still possible, since it is expected that the interface state density is much smaller than in CVD-grown MoTe₂.

In contrast to the 2H-only case, we observed a much stronger modulation of the effective Schottky barrier height for the 2H/1T' device in the high-temperature regime. While we expect the interface state density to be similar for the two cases, the 2H/1T' injector is a pure edge contact, and so the barrier height modulation is not affected by the metal contacts. Therefore, only the interface states associated with the 2H-MoTe₂ play a role in degrading the barrier height modulation.

Finally, we note that the energy barrier for the low-temperature regime of the 2H/1T' device (also shown in Figure 7c) is relatively independent of gate voltage, particularly at positive gate voltages, when the device is nearer to the off-state. We believe that this energy is related to interface traps at the MoTe₂/SiO₂ boundary and is not associated with a Schottky barrier height. In the 2H/1T' devices, the observation of this low-temperature activation energy regime is made possible by the low 2H/1T' barrier, which allows sufficient current flow at low temperature. This regime is less easily observable in the 2H-only sample, since at low temperatures the conductivity is near the noise floor of our measurements.

We also performed density functional theory (DFT) calculations of monolayer to five-layer 1T' and 2H-MoTe₂ band structures to estimate the expected band line ups. Details of the DFT calculations are provided in the Methods section and a further description of the results are provided in the Supporting Information (Figures S14 and S15). The DFT calculations confirm the metallic and semiconducting nature of the 1T' and 2H phases, respectively, and show that the Fermi level at the 2H/1T' boundary is within ~ 77 meV of the valence band edge. The calculated Schottky barrier height is much lower than previous calculations for Ti contacts to 2H-MoTe₂,⁵³ which is qualitatively consistent with our observations in Figure 7c. However, we believe that the effect of interface state charging in our samples, as well as the use of a slightly thicker experimental sample than our calculations, makes a truly quantitative comparison with experiment difficult. Nevertheless, the qualitative agreement of our Schottky barrier height with backgate voltage provides strong evidence as to the high-quality nature of the 2H/1T' lateral interface in MoTe₂.

CONCLUSION

We have conducted a comprehensive study on the microstructural and electrical properties of *in-situ*-grown lateral 2H/1T'-MoTe₂ homojunction films synthesized by flux-controlled phase engineering. The plan-view and cross-sectional TEM/STEM analyses reveal round near-single-crystalline 2H-MoTe₂ domains which stitch seamlessly to the textured polycrystalline 1T'-MoTe₂ matrix. MoTe₂ FETs with metal contacts to 1T' regions show significant improvement in device performance compared to the ones with metal/2H contacts because of the reduced contact resistance and the small barrier height at the 2H/1T' interface. Further reduction of interface traps should lead to improved device performance as well as improved understanding of the transport across the 2H/1T' interface. While in this work, the technique of growing the 1T' and 2H phases

simultaneously is useful for evaluating the barrier heights and interface quality for homojunctions grown using the flux-controlled method, this technique can also be used to grow the two phases sequentially, which could be more practical for FET applications. In such a technique, the channel 2H phase MoTe₂ would be first grown over the entire substrate and patterned into individual channels, followed by the growth of the 1T' phase around the channels, which could be further patterned and deposited with metal contacts. Future work is needed to understand the properties at the sequentially-grown 2H/1T' interface. Finally, MoTe₂ with 2H/1T' built-in homojunctions could also have significant benefits for realizing phase-change memory and logic devices, and recent work has shown that electrostatically-induced phase change is possible through electrostatic gating.³³

METHODS

Synthesis details of lateral 2H/1T' MoTe₂ homojunctions. Mo nanoislands were deposited on SiO₂/Si substrates using electron beam deposition. The Mo nanoislands are about 1-3 nm high and a few hundred nanometers wide. Te lumps was prepared by annealing Te slugs (0.8g, 99.999%, Sigma-Aldrich) at 635 °C for an hour under Ar environment. Mo nanoislands on SiO₂/Si substrates were placed face-down on an alumina boat containing Te lump placed at the center of the heating zone in a 3-inch quartz tube (MTI Corporation). After the quartz tube was evacuated to less than 100 mTorr, Ar flowed at a rate of 500 sccm until the pressure reached atmospheric pressure. At atmospheric pressure, Ar and H₂ flowed at rates of 5 and 5 sccm, respectively. The furnace was ramped to 585 °C in 15 minutes (linear ramp rates ~37.3 °C/min) and was kept at that temperature for an hour for the synthesis of lateral 2H/1T' MoTe₂ few layers. After the reactions, the furnace was rapidly cooled down to room temperature with the furnace lid open.

Sample preparation for cross-sectional TEM. A FEI Nova NanoLab 600 dual-beam (SEM/FIB) scanning electron microscopy and focused ion beam system was employed to prepare the cross-sectional transmission electron microscopy (TEM) samples. SEM was utilized to identify regions of 2H-MoTe₂ and 1T′-MoTe₂ (due to the electron channeling response of nanocrystalline and single crystals). A region of 20 μm in length across the 2H-MoTe₂ / 1T′-MoTe₂ boundary was chosen for lamellar TEM sample preparation. Electron-beam induced deposition of 100-nm-thick Pt was initially deposited on top of the film to protect the sample surface, then followed by 2-μm ion-beam induced Pt deposition. To reduce Ga-ions damage, in the final stage of FIB preparation, the TEM sample was thinned with 2 kV Ga-ions using a low beam current of 29 pA and a small incident angle of 3°.

Sample preparation for plan-view TEM. To prepare the sample for plan-view TEM, the as-grown MoTe₂ homojunction film on a SiO₂/Si substrate was spin-coated with poly(methyl methacrylate) (950 ka.u. PMMA C4) at 3000 rpm for 60 s, followed by 2 min annealing at 100 °C. The sample was then cut into small pieces with sizes slightly larger than that of a mesh copper TEM grid with a lacey carbon film (Ted Pella Product No. 01894). The small pieces were then floated on a 6:1 buffered oxide etch (BOE) solution at room temperature for ~15-20 min until the MoTe₂ films with PMMA were completely detached from the substrates (four sides of the pieces were scratched off with tweezers for BOE etchant access). Next, the MoTe₂ films with PMMA were rinsed in DI water three times (~5 min/each) and transferred onto the mesh copper grids. After the films dried out on the grids, the grids were gently placed in acetone with self-closing tweezers to remove PMMA and rinsed in IPA. The transfer flow chart and images of the transferred films on TEM grids are provided in the Supporting Information.

TEM characterization. A FEI Titan 80-300 STEM/TEM equipped with a probe spherical-aberration corrector was employed to obtain electron diffraction patterns (EDPs), diffraction-contrast imaging (DFI), high resolution transmission electron microscopy (HRTEM) and scanning transmission electron microscopy (STEM) imaging. Atomic-resolution annular dark field (ADF) STEM images were acquired with an operating voltage of 300 kV, probe convergence semi-angle of 14 mrad and collection angle of 34-195 mrad. Low magnification low-angle annular dark field (LAADF) STEM images were acquired with a collection angle of 22-128 mrad, to better differentiate the 2H-MoTe₂ and 1T'-MoTe₂ phases in the plan-view samples.

MoTe₂ FET fabrication and electrical characterization. The MoTe₂ field-effect transistors were fabricated on a Si substrate with 300 nm SiO₂ grown on top, upon which lateral few-layer 2H/1T' mixed-phase MoTe₂ was grown. Alignment marks were first patterned on the substrate by coating poly(methyl methacrylate) (950 ka.u. PMMA C4) and exposing PMMA with electron beam lithography (Vistec EBPG 5000+ system). After development in methyl isobutyl ketone (MIBK)/isopropyl alcohol (IPA) (1:3) and rinsing with IPA, Cr/Au (10 nm/35 nm) was evaporated using electron beam deposition (CHA SEC-600) followed by a liftoff in acetone/IPA. Then, the channel regions (1T', 2H, 2H/1T') were patterned and developed using the same method. After development, exposed flake regions were etched in a 30% H₂O₂ solution for 5 min followed by an acetone/IPA rinse. Finally, source and drain contacts were patterned and developed using the same method as above. After development in MIBK/IPA (1:3), Ti/Au (10 nm/80 nm) was evaporated using electron beam deposition (CHA SEC-600) and lifted off in acetone overnight to complete the device fabrication. The sample was finally cleaned with IPA and loaded into a cryogenic vacuum probe station (Lakeshore CPX-VF) for device

characterization. No annealing was performed. Electrical measurements were performed in the vacuum probe station at $\sim 10^{-6}$ Torr using a Keysight B1500A semiconductor parameter analyzer.

Interface traps density calculation. The interface traps density is extracted from the minimum subthreshold swing (SS). SS is extracted by taking the derivative of the I_D - V_{GS} curves and taking the reciprocal of the derivatives. Then the interface traps capacitance, C_{it} , can be extracted from the minimum SS by $SS = \ln(10) \times (k_BT/q) \times (1 + C_{it}/C_{ox})$. The interface trap density, D_{it} , can be approximately calculated by $D_{it} = C_{it}/q$.

Computational details. Density functional theory (DFT) calculations were performed using the projected-augmented wave (PAW) pseudopotential method⁵⁴ as implemented in the Vienna *ab-initio* simulation package (VASP).⁵⁵ We included van der Waals corrections and spin-orbit coupling in the calculations. We chose the Perdew-Burke-Ernzerhof (PBE) functional⁵⁶ within the generalized gradient approximation (GGA) to treat the exchange-correlation interaction of electrons. The plane-wave kinetic-energy cutoff was set at 300 eV.

A set of (21 × 21 × 1) k-point sampling is used for Brillouin zone (BZ) integration in k-space. All atomic positions were optimized using the conjugate gradient method, where the total energy and atomic forces were minimized. The energy convergence value between two consecutive steps of 10⁻⁶ eV was chosen and a maximum force of 0.001 eV/Å was allowed on each atom. A minimum of 15 Å vacuum spacing was added along the direction perpendicular to the 2D plane, in order to avoid the interaction between the adjacent supercells. While applying electric field, a dipole correction was applied to avoid spurious dipole interactions.⁵⁷

ASSOCIATED CONTENT

Supporting Information. The Supporting Information is available free of charge on the ACS Publications website.

AFM height image of homojunction; sample preparation for plan-view TEMs; indexed polycrystalline diffraction rings of 1T'-MoTe₂; table of experimental and theoretical radiuses of diffraction rings of 1T' MoTe₂; TEM/STEM of the thickness variation and misorientation in the 2H region; field-effect hole mobility at different temperatures; temperature-dependent device behavior for another set of 2H-only and 2H/1T' devices; table of number of devices of each type on samples from different growths; device performance statistics; effective Schottky barrier height extraction; comparison of $V_{\rm BG}$ -dependent effective Schottky barrier heights for different devices; effective Schottky barrier height statistics; flat-band barrier extraction at the 2H/1T' interface; band diagrams for the metal/2H and 2H/1T' interfaces under different bias conditions; band structures of 2H and 1T' MoTe₂; band gap of 2H MoTe₂ and barrier height at the 2H/1T' interface vs. number of layers.

ACKNOWLEDGMENTS

S.J.K. and R.M. were supported by the Defense Threat Reduction Agency Basic Research through award no. HDTRA1-14-1-0042 and partially by the National Science Foundation (NSF) through the University of Minnesota MRSEC under award no. DMR-1420013. J.G.A. and T.L. were supported by the NSF through award no. ECCS1542202. Parts of this work were carried out in the Characterization Facility, University of Minnesota, which has received capital equipment funding from the NSF through the MRSEC program under award no. DMR-1420013. Portions of this work were also conducted in the Minnesota Nano Center, which is supported by the NSF through the National Nanotechnology Coordinated Infrastructure (NNCI) under award no. ECCS-1542202. We acknowledge computational support from the Minnesota

Supercomputing Institute (MSI). The TEM characterization was carried out by H.Z., L.A.B., and A.V.D. at the National Institute of Standards and Technology (NIST). A.V.D. acknowledges the support of Material Genome Initiative funding allocated to NIST. H.Z. acknowledges support from the U.S. Department of Commerce, NIST under the financial assistance award no. 70NANB17H249. Y.Y. was supported by the NRF grants funded by the MSIT (award nos. 2018R1C1B5044670 and 2019R1C1C1008070). P. G. was supported by the NSF through award no. ECCS-1708769.

Table 1. Comparison of 2H-only and 2H/1T' device performance

| Property | 2H-only devices | 2H/1T' devices | Ratio |
|--|--------------------|-------------------|-------|
| On-current (nA/ μ m) (at 300 K, $V_{BG} = -100$ V, $V_{DS} = -0.1$ V) | 5.72 | 39.6 | 6.9 |
| Transconductance (nS/ μ m) (at 300 K, $V_{DS} = -0.1$ V) | 0.2 | 0.43 | 2.1 |
| Field-effect hole mobility (cm ² V ⁻¹ s ⁻¹) (at 300 K, $V_{DS} = -0.1$ V) | 0.6-0.8 | 7-8 | 9-13 |
| Current on/off ratio (at 77 K, $V_{DS} = -0.1 \text{ V}$) | 10 | 3.5×10^3 | 350 |

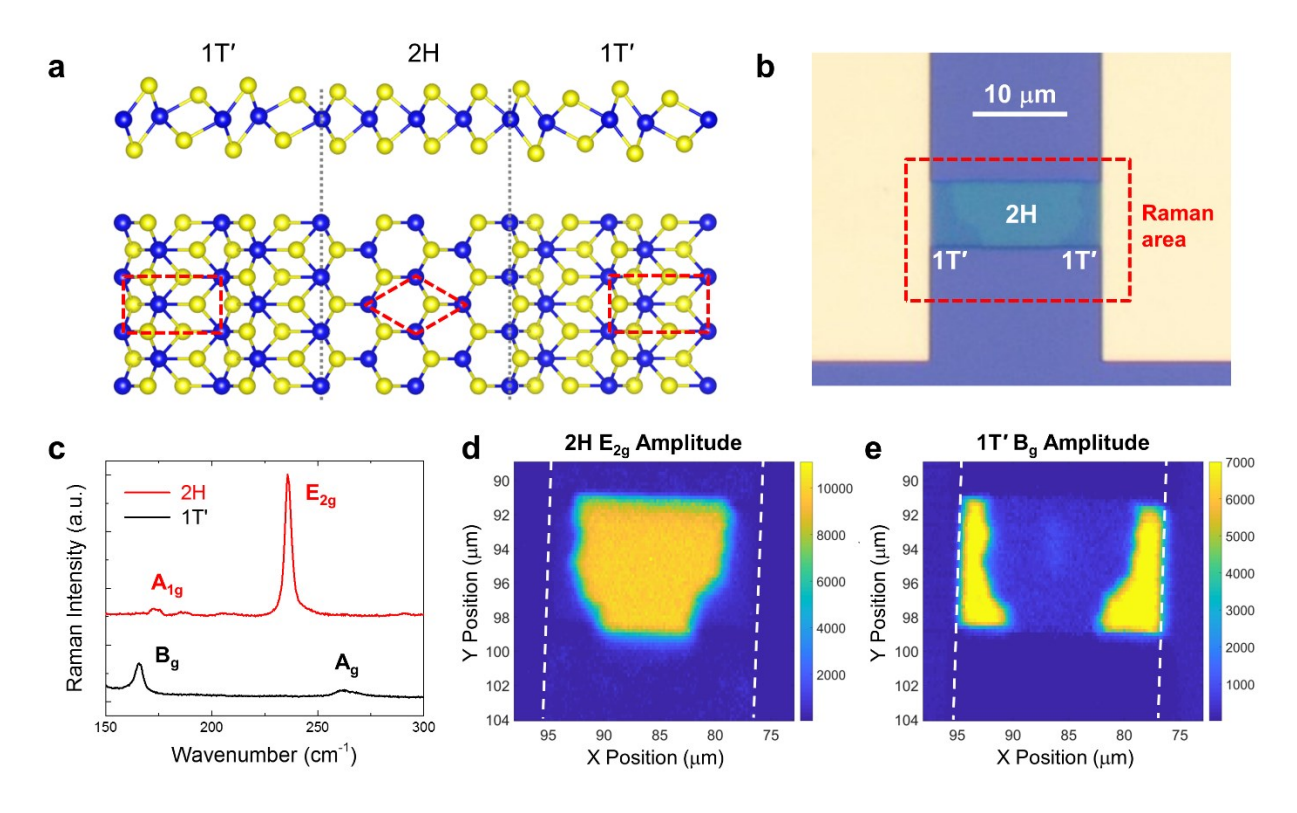


Figure 1. Crystal structure model and Raman mapping of 2H/1T' MoTe₂. (a) Schematic diagram of an in-plane monolayer 2H/1T' MoTe₂ homojunction. The top is a cross-sectional view and the bottom is basal plane view. The blue spheres are Mo atoms and the yellow spheres are Te atoms. The red dashed boxes represent the primitive unit cells. (b) Optical image of a 2H/1T' device. Both the 1T' and 2H-MoTe₂ films are \sim 6-nm thick in this region. (c) Raman spectra taken from the 1T' and 2H regions in (b) with an excitation laser with a wavelength of 633 nm and a power of $150~\mu W$. (d)-(e) Raman intensity maps of the E_{2g} mode of the 2H phase and the B_g mode of the 1T' phase of the region in the red rectangle in (b). White dashed lines are the borders of the contact fingers.

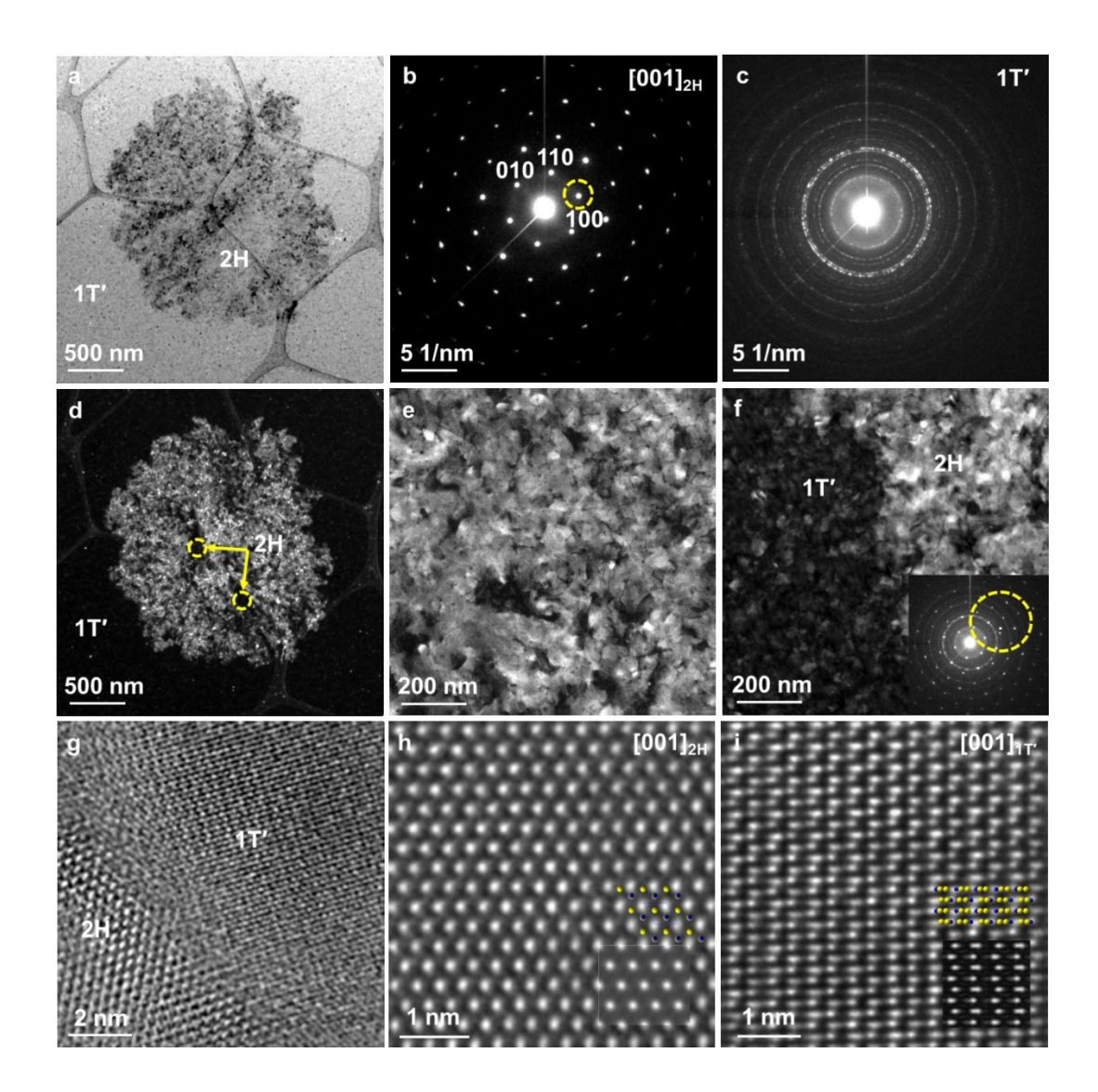


Figure 2. Plan-view TEM characterization results of as-grown the 2H/1T' MoTe₂ homojunction. (a) Low-magnification bright-field TEM image showing the round region of 2H phase surrounded by the 1T' phase matrix. (b)-(c) Selected-area electron diffraction patterns from the round region and matrix showing the near-single-crystal pattern of the 2H phase and polycrystalline diffraction rings of the 1T' phase, respectively. (d) Dark-field image with an aperture at the (100) diffraction spot in (b) showing the well-defined 2H/1T' interface, and (e) zoomed-in image demonstrating local structural variation in the 2H phase. (f) Dark-field image taken from the 2H/1T' interface region with a large aperture (placed as shown in the inset) showing the polycrystalline 1T' grains. (g) HRTEM image showing structural continuity at the homojunction. (h)-(i) HRTEM images with insets of projected atomic models and corresponding simulated HRTEM images showing good match with the hexagonal and orthorhombic structures of 2H and 1T' along their [001] zone-axis, respectively.

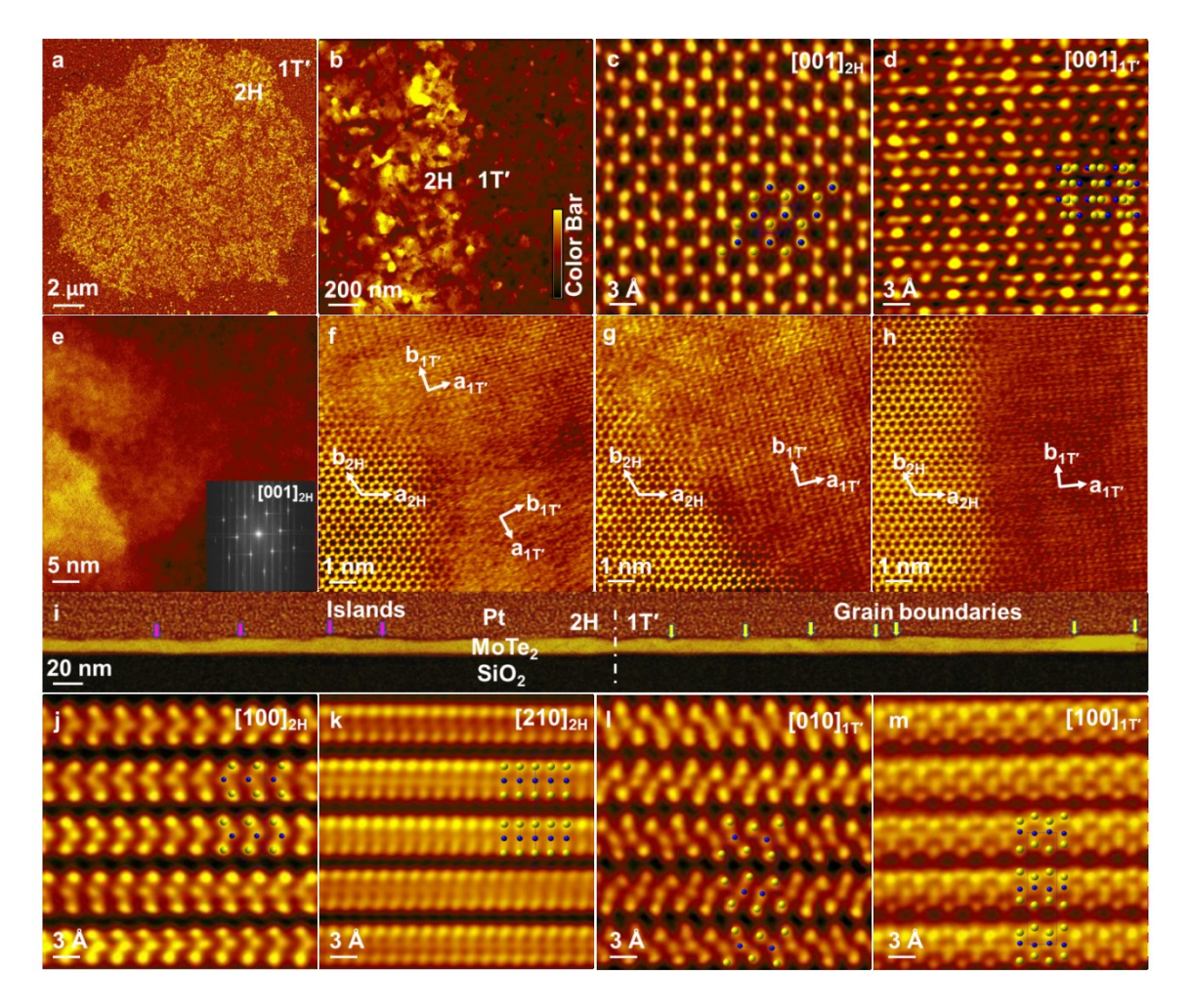


Figure 3. STEM characterization of plan-view/cross-sectional samples of as-grown 2H/1T′ MoTe₂ homojunction. (a) Low magnification LAADF-STEM image showing the round 2H region surrounded by the 1T′ matrix in the plan-view sample. (b) Zoomed-in LAADF-STEM image showing mottled contrast in the 2H region and the polycrystalline 1T′ matrix. (c)-(d) Typical HRSTEM images with matching atomic projections of the corresponding 2H and 1T′ phases, respectively. (e) HRSTEM image of a large area from the mottled 2H region with the corresponding FFT image in the inset. (f)-(h) HRSTEM images showing the 2H connecting seamlessly with the neighboring randomly orientated 1T′ grains. (i) Low magnification cross-sectional STEM image showing the thickness variations in the 2H region and grain boundaries in the 1T′ region. (j)-(m) Typical HRSTEM images taken from the 2H (j)-(k) and 1T′ (l)-(m) regions. False colors are added to aid the eye.

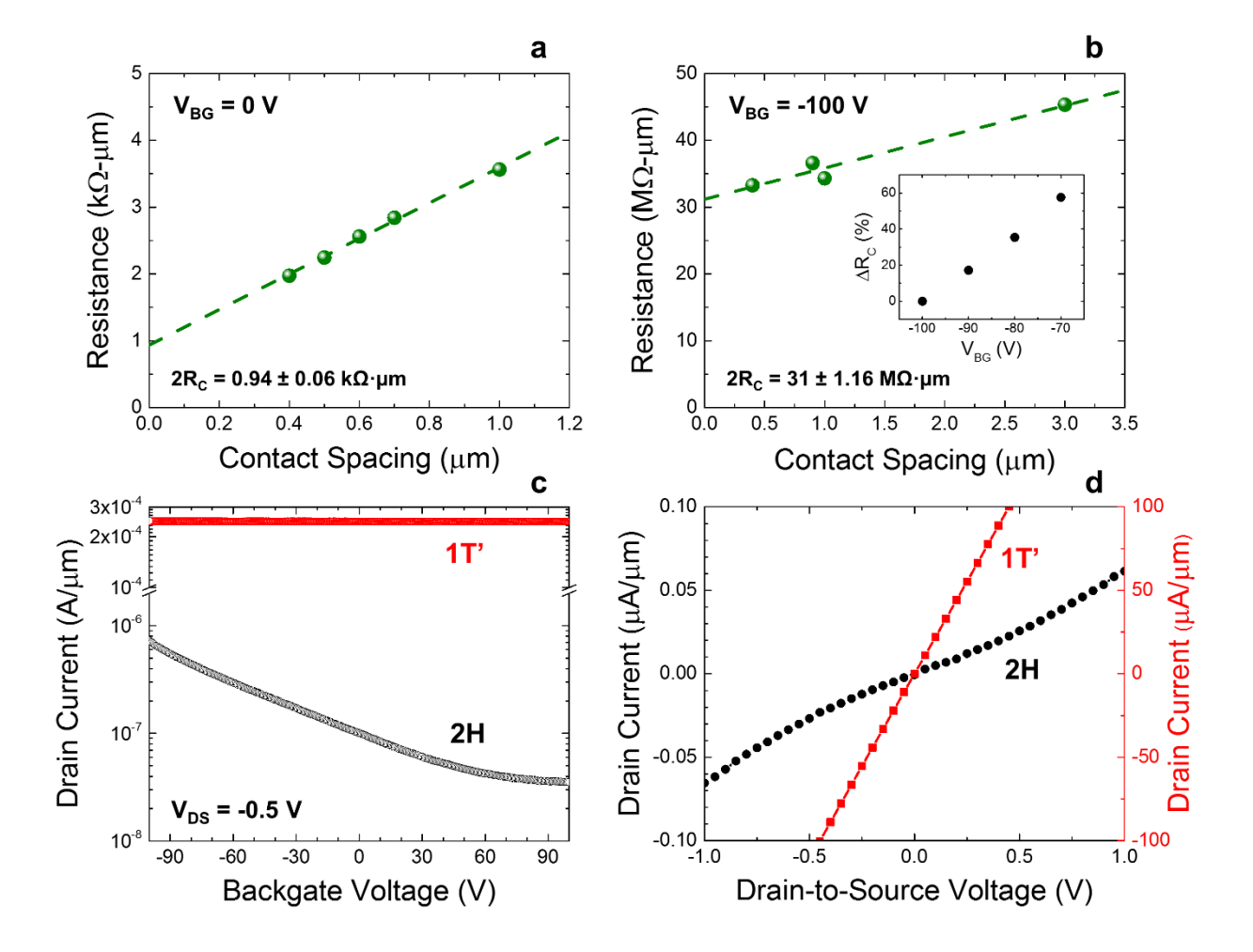


Figure 4. Transfer length measurements and device characteristics. (a) Resistance vs. contact spacing for the 1T'-only device at $V_{\rm BG} = 0$ V. (b) Resistance vs. contact spacing for the 2H-only device at $V_{\rm BG} = -100$ V. Inset is the percentage change of contact resistance at different $V_{\rm BG}$. (c) Room-temperature transfer characteristics of the 1T'-only and 2H-only devices at $V_{\rm DS} = -0.5$ V. (d) Room-temperature output characteristics of the 1T'-only device at $V_{\rm BG} = 0$ V and the 2H device at $V_{\rm BG} = -100$ V.

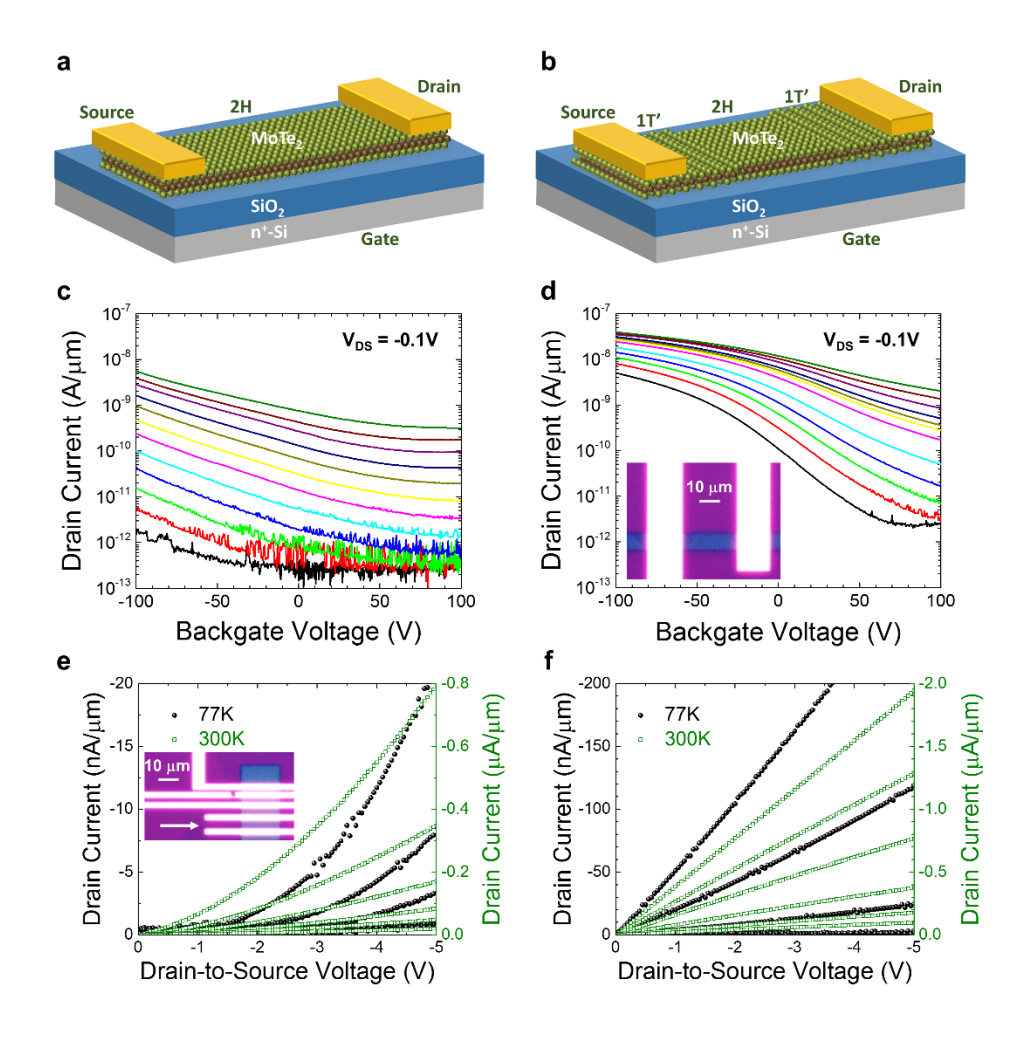


Figure 5. Temperature-dependent transport characteristics of the 2H-only and 2H/1T' devices. (a)-(b) Schematic diagram of (a) 2H-only and (b) 2H/1T' device structures. The dimensions of the 2H-only device are $L_{\rm DS}=3~\mu {\rm m}$ and $W=21~\mu {\rm m}$, while the 2H/1T' device has $L_{\rm DS}=23~\mu {\rm m}$ and $W=9~\mu {\rm m}$ (the length of the 2H region is about 18 $\mu {\rm m}$). (c)-(d) Transfer characteristics ($I_{\rm D}~vs$. $V_{\rm BG}$) of (c) 2H-only device and (d) 2H/1T' device at $V_{\rm DS}=-0.1{\rm V}$ for temperatures of 77 K (black curve), and from 100 K (red curve) to 300 K (olive curve), in steps of 20 K. (e)-(f) Output characteristics ($I_{\rm D}~vs$. $V_{\rm DS}$) of 2H-only and 2H/1T' device for $V_{\rm BG}$ varying from -100V (top curve) to +100V (bottom curve) in steps of +40 V at $T=77{\rm K}$ (black points) and $T=300~{\rm K}$ (olive points). The optical images of the 2H-only and the 2H/1T' devices are inset in (e) and (d), respectively, where the specific device is indicated by the arrow.

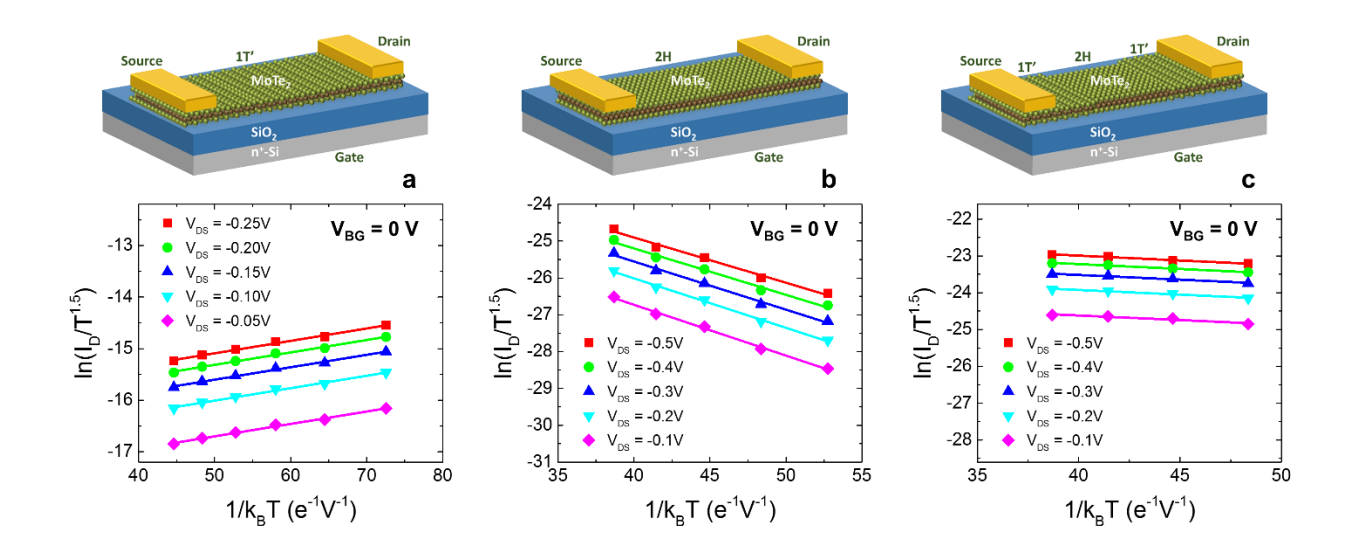


Figure 6. Arrhenius plots and bias-dependent effective barrier heights in the high temperature regime. (a) Arrhenius plots of $\ln(I_{\rm D}/T^{1.5})$ vs. $1/k_{\rm B}T$ for the 1T'-only device (depicted at the top) at $V_{\rm BG}=0$ for different values of $V_{\rm DS}$. The positive slopes indicate the absence of an energy barrier at the metal/1T' interface. (b) Arrhenius plots for the 2H-only device at $V_{\rm BG}=0$ V for different values of $V_{\rm DS}$. (c) Arrhenius plots for the 2H/1T' device at $V_{\rm BG}=0$ V for different values of $V_{\rm DS}$. Given the absence of a barrier at the metal/1T' interface, the slope is an indication of the barrier height at the 2H/1T' interface.

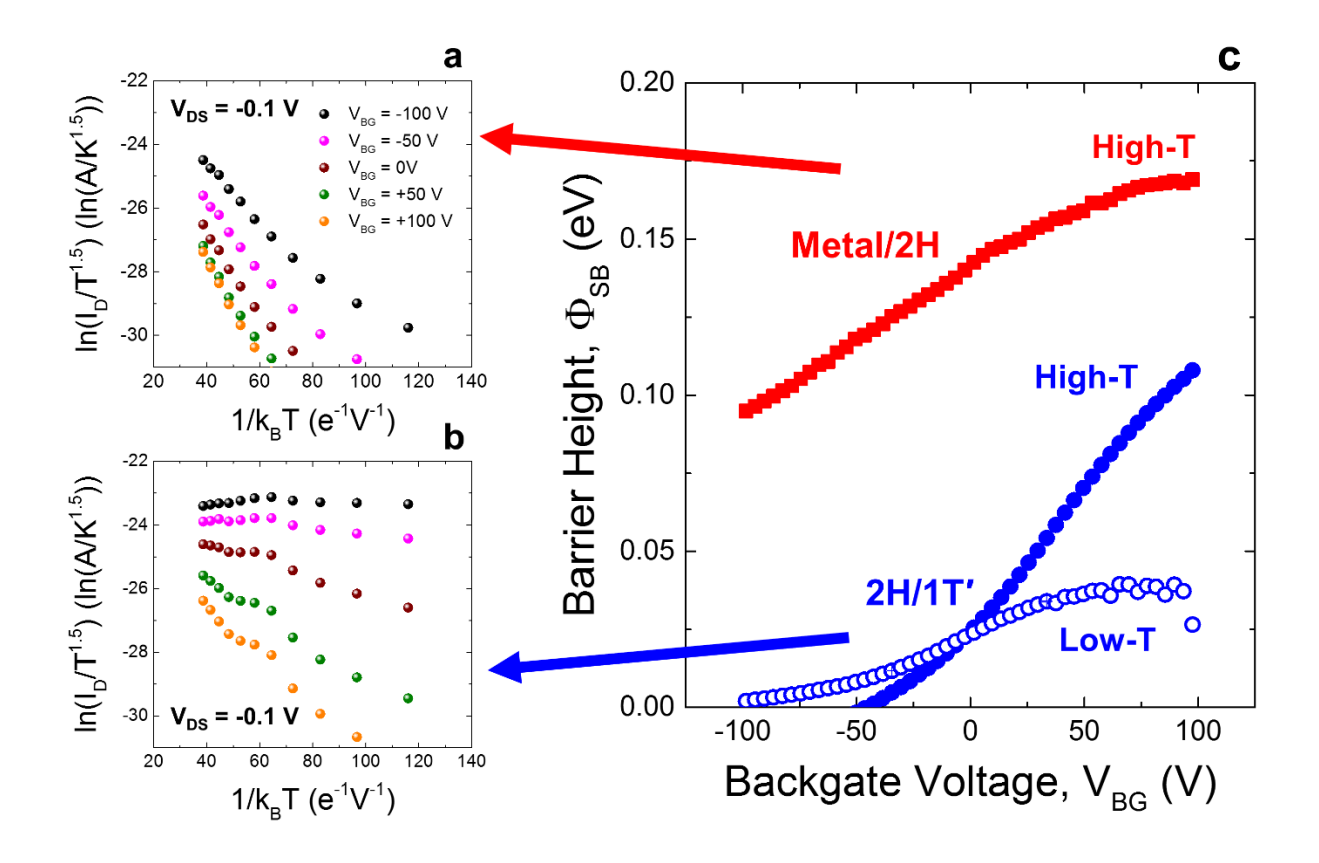
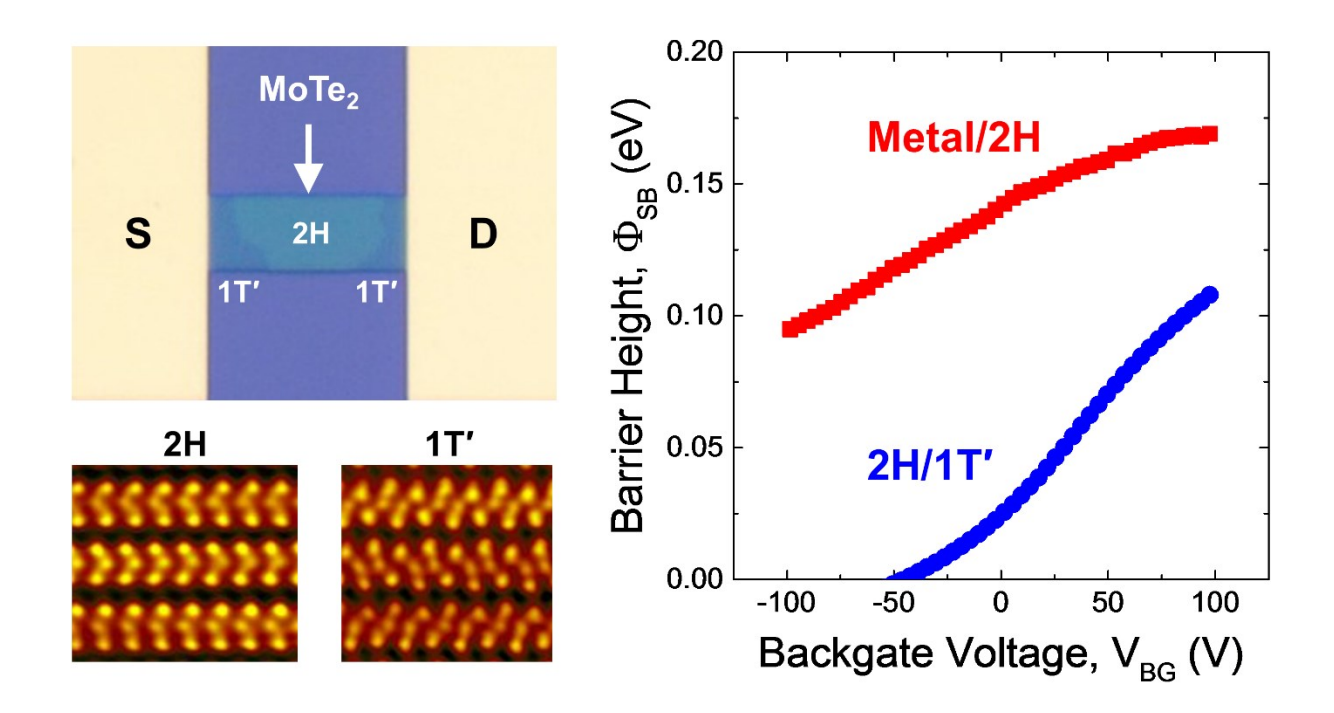


Figure 7. Backgate voltage dependent Arrhenius plots and effective Schottky barrier heights. (a)-(b) Arrhenius plots for the (a) 2H-only device and (b) 2H/1T' device at $V_{DS} = -0.1$ V for V_{BG} ranging from -100 V to 100 V. (c) Effective Schottky barrier height of the 2H-only device in the high temperature regime (red squares) and 2H/1T' device in the high- (close blue circles) and low- (open blue circles) temperature regimes as a function of V_{BG} .



For Table of Contents Only

REFERENCES

- Wang, H.; Yu, L.; Lee, Y. H.; Shi, Y.; Hsu, A.; Chin, M. L.; Li, L. J.; Dubey, M.; Kong, J.; Palacios, T. Integrated Circuits Based on Bilayer MoS₂ Transistors. *Nano Lett.* **2012**, *12*, 4674-4680.
- Wang, H.; Yu, L.; Lee, Y.-H.; Fang, W.; Hsu, A.; Herring, P.; Chin, M.; Dubey, M.; Li, L.-J.; Kong, J.; Palacios, T. Large-Scale 2D Electronics Based on Single-Layer MoS₂ Grown by Chemical Vapor Deposition, *IEDM* **2012**, 4.6.1-4.6.4.
- Su, Y.; Kshirsagar, C. U.; Robbins, M. C.; Haratipour, N.; Koester, S. J. Symmetric Complementary Logic Inverter Using Integrated Black Phosphorus and MoS₂ Transistors. *2D Mater.* **2016**, *3*, 011006.
- 4 Liu, E.; Fu, Y.; Wang, Y.; Feng, Y.; Liu, H.; Wan, X.; Zhou, W.; Wang, B.; Shao, L.; Ho, C.-H.; Huang, Y.-S.; Cao, Z.; Wang, L.; Li, A.; Zeng, J.; Song, F.; Wang, X.; Shi, Y.; Yuan, H.; Hwang, H. Y.; et al. Integrated Digital Inverters Based on Two-Dimensional Anisotropic ReS₂ Field-Effect Transistors. Nat. Commun. 2015, 6, 6991.
- 5 Kshirsagar, C. U.; Xu, W.; Su, Y.; Robbins, M. C.; Kim, C. H.; Koester, S. J. Dynamic Memory Cells Using MoS₂ Field-Effect Transistors Demonstrating Femtoampere Leakage Currents. *ACS Nano* **2016**, *10*, 8457-8464.
- Zhang, F.; Zhang, H.; Krylyuk, S.; Milligan, C. A.; Zhu, Y.; Zemlyanov, D. Y.; Bendersky, L. A.; Burton, B. P.; Davydov, A. V.; Appenzeller, J. Electric-Field Induced Structural Transition in Vertical MoTe₂- and Mo_{1-x}W_xTe₂-Based Resistive Memories. *Nat. Mater.* 2019, 18, 55-61.
- Zhang, F.; Zhang, H.; Shrestha, P. R.; Zhu, Y.; Maize, K.; Krylyuk, S.; Shakouri, A.; Campbell, J. P.; Cheung, K. P.; Bendersky, L. A.; Davydov, A. V.; Appenzeller, J. An Ultra-fast Multi-level MoTe₂-based RRAM. *IEDM* **2018**, 22.7.1-22.7.4.
- 8 Lipatov, A.; Sharma, P.; Gruverman, A.; Sinitskii, A. Optoelectrical Molybdenum Disulfide (MoS₂)-Ferroelectric Memories. *ACS Nano* **2015**, *9*, 8089-8098.
- Zhang, E.; Wang, W.; Zhang, C.; Jin, Y.; Zhu, G.; Sun, Q.; Zhang, D.W.; Zhou, P.; Xiu, F.
 Tunable Charge-Trap Memory Based on Few-Layer MoS₂. ACS Nano 2015, 9, 612-619.

- 10 Radisavljevic, B.; Radenovic, A.; Brivio, J.; Giacometti, V.; Kis, A. Single-layer MoS₂ transistors. *Nat. Nanotech.* **2011**, *6*, 147-150.
- Ovchinnikov. D.; Allain, A.; Huang, Y. S.; Dumcenco, D.; Kis, A. Electrical Transport Properties of Single-Layer WS₂. *ACS Nano* **2014**, *8*, 8174-8181.
- 12 Qiu, H.; Pan, L. J.; Yao, Z. N.; Li, J. J.; Shi, Y.; Wang, X. R. Electrical Characterization of Back-Gated Bi-Layer MoS₂ Field-Effect Transistors and the Effect of Ambient on Their Performances. *Appl. Phys. Lett.* 2012, 100, 123104.
- Liu, X.; Hu, J.; Yue, C.; Fera, N. D.; Ling, Y.; Mao, Z.; Wei, J. High Performance Field Effect Transistor Based on Multilayer Tungsten Disulfide. ACS Nano 2014, 8, 10396-10402.
- 14 Kim, S.; Konar, A.; Hwang, W. S.; Lee, J. H.; Lee, J.; Yang, J.; Jung, C.; Kim, H.; Yoo, J.-B.; Choi, J.-Y.; Jin, Y. W.; Lee, S. Y.; Jena, D.; Choi, W.; Kim, K. High-Mobility and Low-Power Thin-Film Transistors Based on Multilayer MoS₂ Crystals. *Nat. Commun.* 2012, 3, 1011.
- Fiori, G.; Bonaccorso, F.; Iannaccone, G.; Palacios, T.; Neumaier, D.; Seabaugh, A.; Banerjee, S. K. Colombo, L. Electronics Based on Two-Dimensional Materials. *Nat. Nanotech.* 2014, 9, 768-779.
- Allain, A.; Kang, J.; Banerjee, K.; Kis, A. Electrical Contacts to Two-Dimensional Semiconductors. *Nat. Mater.* **2015**, *14*, 1195-1205.
- 17 Smyth, C. M.; Addou, R.; McDonnell, S.; Hinkle, C. L.; Wallace, R. M. Contact Metal–MoS₂ Interfacial Reactions and Potential Implications on MoS₂-Based Device Performance. *J. Phys. Chem. C.* **2016**, *120*, 14719-14729.
- Liu, H.; Neal, A.T.; Ye, P.D. Channel Length Scaling of MoS₂ MOSFETs. *ACS Nano* **2012**, 6, 8563-8569.
- Lin, Y.-F.; Xu, Y.; Wang, S.-T.; Li, S.-L.; Yamamoto, M.; Aparecido-Ferreira, A.; Li, W.; Sun, H.; Nakaharai, S.; Jian, W.-B.; Ueno, K.; Tsukagoshi, K. Ambipolar MoTe₂
 Transistors and Their Applications in Logic Circuits. Adv. Mater. 2014, 26, 3263-3269.

- Gong, C.; Colombo, L., Wallace, R. M.; Cho, K. The Unusual Mechanism of Partial Fermi Level Pinning at Metal–MoS₂ Interfaces. *Nano Lett.* **2014**, *14*, 1714-1720.
- Das, S.; Chen, H. Y.; Penumatcha, A. V.; Appenzeller, J. High Performance Multilayer MoS₂ Transistors with Scandium Contacts. *Nano Lett.* **2013**, *13*, 100-105.
- Du, Y.; Liu, H.; Neal, A. T.; Si, M.; Ye, P. D. Molecular Doping of Multilayer MoS₂ Field-Effect Transistors: Reduction in Sheet and Contact Resistances. *IEEE Elect. Dev. Lett.* **2013**, *34*, 1328-1330.
- Harati Pour, N.; Anugrah, Y.; Wu, S.; Xu, X.; Koester, S. J. Chemical Doping for Threshold Control and Contact Resistance Reduction in Graphene and MoS₂ Field Effect Transistors. *71st Dev. Res. Conf.* **2013**, 101-102.
- Tosun, M.; Chan, L.; Amani, M.; Roy, T.; Ahn, G. H.; Taheri, P.; Carrao, C.; Ager, J. W.; Maboudian, R.; Javey, A. Air-Stable *n*-Doping of WSe₂ by Anion Vacancy Formation with Mild Plasma Treatment. *ACS Nano* **2016**, *10*, 6853-6860.
- Du, Y.; Yang, L.; Zhang, J.; Liu, H.; Majumdar, K.; Kirsch, P. D.; Ye, P. D. MoS₂ Field-Effect Transistors with Graphene/Metal Heterocontacts. *IEEE Elect. Dev. Lett.* **2014**, *35*, 599-601.
- Byun, K. E.; Chung, H. J.; Lee, J.; Yang, H.; Song, H. J.; Heo, J.; Seo, D. H.; Parl, S.; Hwang, S. W.; Yoo, I.; Kim, K. Graphene for True Ohmic Contact at Metal–Semiconductor Junctions. *Nano Lett.* 2013, *13*, 4001-4005.
- 27 Leong, W. S.; Luo, X.; Li, Y.; Khoo, K. H.; Quek, S. Y.; Thong, J. T. L. Low Resistance Metal Contacts to MoS₂ Devices with Nickel-Etched-Graphene Electrodes. *ACS Nano* 2015, 9, 869-877.
- Wang, Q. H.; Kalantar-Zadeh, K.; Kis, A.; Coleman, J. N.; Strano, M. S. Electronics and Optoelectronics of Two-Dimensional Transition Metal Dichalcogenides. *Nat. Nanotech.* 2012, 7, 699-712.
- 29 Chhowalla. M.; Shin, H. S.; Eda, G.; Li, L. J.; Loh, K. P.; Zhang, H. The Chemistry of Two-Dimensional Layered Transition Metal Dichalcogenide Nanosheets. *Nat. Chem.* 2013, 5, 263-275.

- Enyashin, A. N.; Yadgarov, L.; Houben, L.; Popov, Igor; Weidenbach, M.; Tenne, R.; Bar-Sadan, M.; Seifert, G. New Route for Stabilization of 1T-WS₂ and MoS₂ Phases. *J. Phys. Chem. C.* **2011**, *115*, 24586-24591.
- Keum, D. H.; Cho, S.; Kim, J. H.; Choe, D. H.; Sung, H. J.; Kan, M.; Kang, H.; Hwang, J. Y.; Kim, S. W.; Yang, H.; Chang, K. J.; Lee, Y. H. Bandgap Opening in Few-Layered Monoclinic MoTe₂. *Nat. Phys.* 2015, *11*, 482-486.
- Li, Y; Duerloo, K. N.; Wauson, K.; Reed, E. J. Structural Semiconductor-to-Semimetal Phase Transition in Two-Dimensional Materials Induced by Electrostatic Gating. *Nat. Commun.* **2016**, *7*, 10671.
- Wang, Y.; Xiao J.; Zhu, H.; Li, Y.; Alsaid, Y.; Fong, K. Y.; Zhou, Y.; Wang, S.; Shi, W.; Wang, Y.; Zettl, A.; Reed, E. J.; Zhang, X. Structural Phase Transition in Monolayer MoTe₂ Driven by Electrostatic Doping. *Nature* 2017, 550, 487-491.
- Cho, S.; Kim, S.; Kim, J. H.; Zhao, J.; Seok, J.; Keum, D. H.; Baik, J.; Choe, D. H.; Chang, K. J.; Suenaga, K.; Kim, S. W.; Lee, Y. H.; Yang, H. Phase Patterning for Ohmic Homojunction Contact in MoTe₂. *Science* 2015, 349, 625-628.
- Song, S.; Keum, D. H.; Cho, S.; Perello, D.; Kim, Y.; Lee, Y. H. Room Temperature Semiconductor–Metal Transition of MoTe₂ Thin Films Engineered by Strain. *Nano Lett.* **2016**, *16*, 188-193.
- Yang, L.; Zhang, W.; Li, J.; Cheng, S.; Xie, Z.; Chang, H. Tellurization Velocity-Dependent Metallic-Semiconducting-Metallic Phase Evolution in Chemical Vapor Deposition Growth of Large-Area, Few-Layer MoTe₂. ACS Nano 2017, 11, 1964-1972.
- Cheng, S.; Yang, L.; Li, J.; Liu, Z.; Zhang, W.; Chang, H. Large Area, Phase-Controlled Growth of Few-Layer, Two-Dimensional MoTe₂ and Lateral 1T'–2H Heterostructures by Chemical Vapor Deposition. *CrystEngComm* **2017**, *19*, 1045-1051.
- Park, J. C.; Yun, S. J.; Kim, H.; Park, J.-H.; Chae, S. H.; An, S.-J.; Kim, J.-G.; Kim, S. M.; Kim, K. K.; Lee, Y. H. Phase-Engineered Synthesis of Centimeter-Scale 1T'- and 2H-Molybdenum Ditelluride Thin Films. ACS Nano 2017, 9, 6548-6554.

- Sung, J. H.; Heo, H.; Si, S.; Kim, Y. H.; Noh, H. R.; Song, K.; Kim, J.; Lee, C. S.; Seo, S. Y.; Kim, D. H.; Kim, H. K.; Yeom, H. W.; Kim, T.-H.; Choi, S.-Y.; Kim, J. S.; Jo, M.-H.. Coplanar Semiconductor-Metal Circuitry Defined on Few-Layer MoTe2 via Polymorphic Heteroepitaxy. Nat. Nanotechnol. 2017, 12, 1064-1070.
- 40 Yoo, Y; DeGregorio, Z. P.; Su, Y.; Koester, S. J.; Johns, J. E. In-Plane 2H-1T' MoTe₂ Homojunctions Synthesized by Flux-Controlled Phase Engineering. *Adv. Mater.* **2017**, *29*, 1605461.
- 41 Xu, X.; Chen, S.; Liu, S.; Cheng, X.; Xu, W.; Li, P.; Wan, Y.; Yang, S.; Gong, W.; Yuan, K.; Gao, P.; Ye, Y.; Dai, L. Millimeter-Scale Single-Crystalline Semiconducting MoTe₂ via Solid-to-Solid Phase Transformation. J. Am. Chem. Soc. 2019, 141, 5, 2128-2134.
- 42 Zhu, X.; Li, D.; Liang, X.; Lu, W. D. Ionic Modulation and Ionic Coupling Effects in MoS₂
 Devices for Neuromorphic Computing. *Nat. Mater.* **2019**, *18*, 141-148.
- Zheng, F.; Zhang, H.; Krylyuk, S.; Milligan, C. A.; Zhu, Y.; Zemlyanov, D. Y.; Bendersky, L. A.; Burton, B. P.; Davydov, A. V.; Appenzeller, J. Electric-Field Induced Structural Transition in Vertical MoTe₂- and Mo_{1-x}W_xTe₂-based Resistive Memories. *Nat. Mater.*2019, 18, 55-61.
- 44 Yang, D.; Hu, X.; Zhuang, M.; Ding, Y.; Zhou, S.; Li, A.; Yu, Y.; Li, H.; Luo, Z.; Gan, L.; Zhai, T. Inversion Symmetry Broken 2D 3R-MoTe₂. *Adv. Funct. Mater.***2018**, 28, 1800785.
- Kappera, R.; Voiry, D.; Yalcin, S. E.; Branch, B.; Gupta, G.; Mohite, A. D.; Chhowalla, M.
 Phase-Engineered Low-Resistance Contacts for Ultrathin MoS₂ Transistors. *Nat. Mater.* 2014, 13, 1128-1134.
- Zhang, X.; Jin, Z.; Wang, L.; Hachtel, J. A.; Villarreal, E.; Wang, Z.; Ha, T.; Nakanishi, Y.;
 Tiwary, C. S.; Lai, J.; Dong, L.; Yang, J.; Vajtai, R.; Ringer, E.; Idrobo, J. C.; Yakobson, B.
 I.; Luo, J.; Gambin, V.; Koltun, R.; Ajayan, P. M. Low Contact Barrier in 2H/1T' MoTe₂
 In-Plane Heterostructure Synthesized by Chemical Vapor Deposition. *ACS Appl. Mater.*Interfaces 2019, 11, 12777-12785.

- Fathipour, S.; Ma, N.; Hwang, W. S.; Protasenko, V.; Vishwanath, S.; Xing, H. G.; Xu, H.; Jena, D.; Appenzeller, J.; Seabaugh, A. Exfoliated Multilayer MoTe₂ Field-Effect Transistors. *Appl. Phys. Lett.* **2014**, *105*, 192101.
- Haratipour, N.; Koester, S. J. Multi-Layer MoTe₂ *p*-Channel MOSFETs with High Drive Current. 72nd Device Research Conference (DRC), Santa Barbara, CA, Jun. 22-25, 2014.
- 49 Prakash, A.; Ilatikhameneh, H.; Wu P.; Appenzeller, J. Understanding Contact Gating in Schottky Barrier Transistors from 2D Channels. *Sci. Rep.* **2017**, *7*, 12596.
- Nagashio, K.; Nishimura, T.; Kita, K.; Toriumi, A. Contact Resistivity and Current Flow Path at Metal/Graphene Contact. *Appl. Phys. Lett.* **2010**, *97*, 143514.
- Grosse, K. L.; Bae, M.-H.; Lian, F.; Pop, E.; King, W. P. Nanoscale Joule Heating, Peltier Cooling and Current Crowding at Graphene-Metal Contacts. *Nat. Nanotechnol.* **2011**, *6*, 287-290.
- Guo, Y.; Han, Y.; Li, J.; Xiang, A.; Wei, X.; Gao, S.; Chen, Q. Study on the Resistance Distribution at the Contact between Molybdenum Disulfide and Metals. *ACS Nano* **2014**, *8*, 7771-7779.
- Kim, C.; Moon, I.; Lee, D.; Choi, M. S.; Ahmed, F.; Nam, S.; Cho, Y.; Shin, H. J.; Park, S.; Yoo, W. J. Fermi Level Pinning at Electrical Metal Contacts of Monolayer Molybdenum Dichalcogenides. ACS Nano 2017, 11, 1588-1596.
- 54 Blöchl, P. E. Projector Augmented-Wave Method. *Phys. Rev. B* **1994**, *50*, 17953-17979.
- Kresse, G.; Furthmüller, J. Efficient Iterative Schemes for *Ab-Initio* Total Energy Calculations Using a Plane-Wave Basis Set. *Phys. Rev. B* **1996**, *54*, 11169-11186.
- Perdew, J. P.; Burke, K.; Ernzerhof, M. Generalized Gradient Approximation Made Simple. *Phys. Rev. Lett.* **1996**, *77*, 3865-3868.
- 57 Makov, G.; Payne, M. C. Periodic Boundary Conditions *in Ab Initio* Calculations. *Phys. Rev. B.* **1995**, *51*, 4014-402.

Supporting Information for

MoTe₂ Lateral Homojunction Field-Effect Transistors Fabricated using Flux-Controlled Phase Engineering

Rui Ma,¹ Huairuo Zhang,²,³* Youngdong Yoo,⁴ Zachary Patrick Degregorio,⁵ Lun Jin,⁵ Prafful Golani,¹ Javad Ghasemi Azadani,¹ Tony Low,¹ James E. Johns,⁵ Leonid A. Bendersky,³ Albert V. Davydov,³ and Steven J. Koester¹*

¹Dept. of Electrical & Computer Engineering, University of Minnesota, Minneapolis, MN 55455, USA

²Theiss Research, Inc., La Jolla, California 92037, USA

³Materials Science and Engineering Division, National Institute of Standards and Technology (NIST), Gaithersburg, MD 20899, USA

⁴Department of Chemistry, Ajou University, Suwon 16499, Korea

⁵Department of Chemistry, University of Minnesota, Minneapolis, MN 55455, USA

*Corresponding Authors: skoester@umn.edu (S.J.K.); huairuo.zhang@nist.gov (H.Z.)

1. AFM height image of homojunction:

AFM measurements were performed on a MoTe₂ homojunction grown on a SiO₂/Si substrate, as shown in Figure S1a. The AFM height map of the region in the red dashed box is shown in Figure S1b. The height profile in Figure S1c across the homojunction (line 2 in Figure S1b) indicates that there is no systematic change in height across the homojunction, which is consistent with the cross-sectional TEM result at the 2H/1T' interface in Figure 3 of the manuscript. The boundary between two phases is still slightly visible in the height map (Figure S1b), which we attribute to the local variations in the texturing of the 1T' and 2H regions. The height profile in Figure S1d across the film edge (line 1 in Figure S1b) shows that the thickness of the film is around 8 nm.

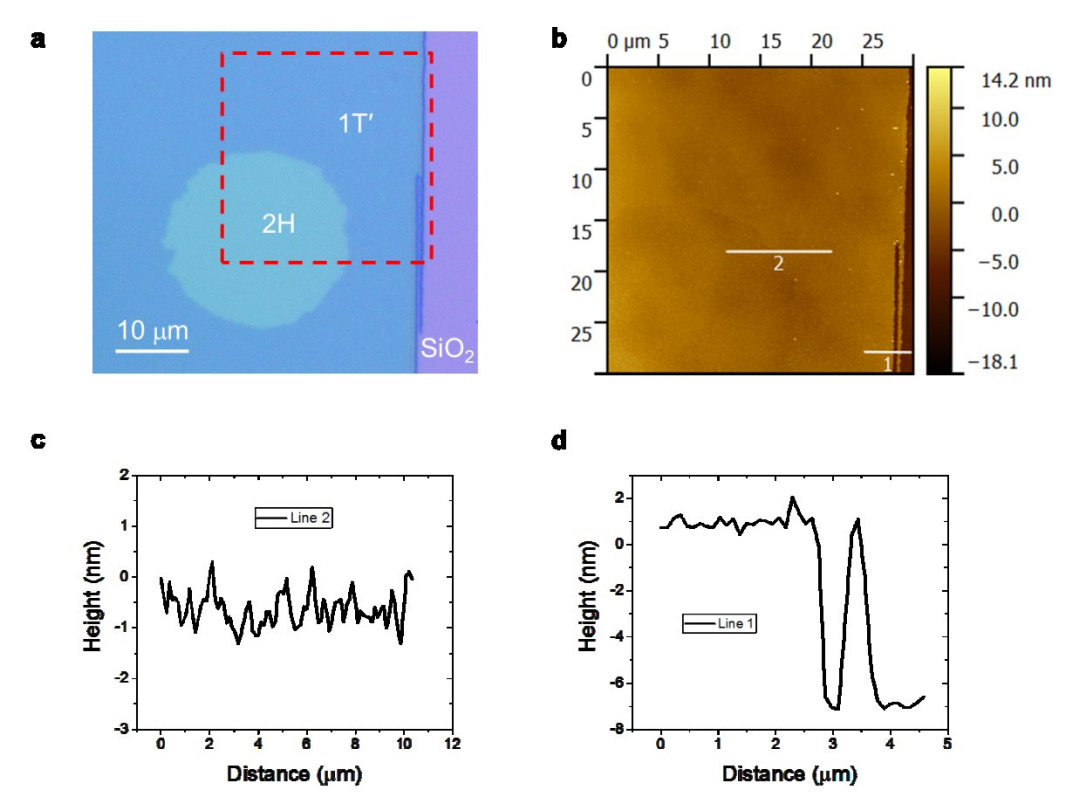


Figure S1. (a) Optical image of a MoTe₂ homojunction grown on a SiO₂/Si substrate. The right side was scratched off by tweezers. (b) AFM height map of the region in the red dashed box in (a). (c) The height profile along the horizontal white line 2 showing no significant height difference across the homojunction. (d) Height profile along the horizontal white line 1 in (b) showing that the thickness of the film is 8 nm.

2. Sample preparation for plan-view TEMs:

The plan-view sample preparation method is described below in Figure S2.

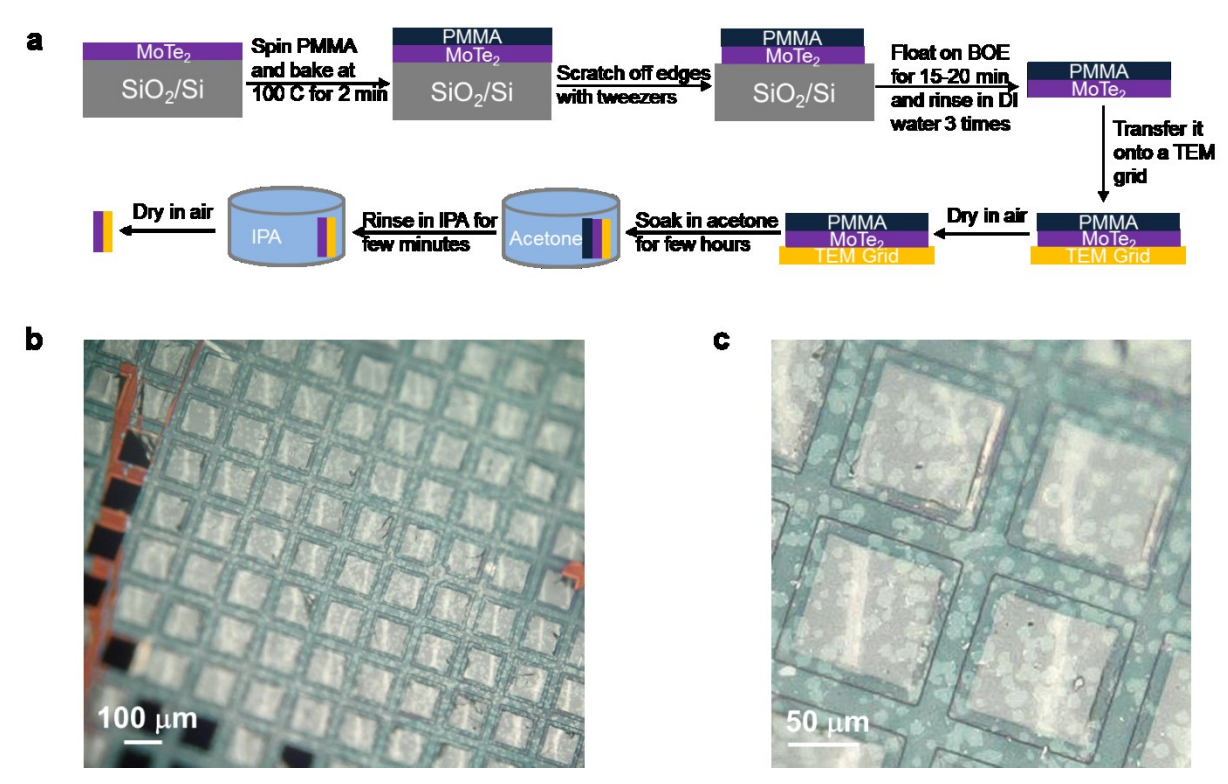


Figure S2. (a) Sample preparation process for plan-view TEM. Zoom-out image (b) and zoom-in image (c) of a transferred MoTe₂ homojunction film on copper TEM grid with a lacey carbon film. The grid has good coverage.

3. Indexed polycrystalline diffraction rings of 1T'-MoTe₂:

The selected area electron diffraction pattern in Figure 2c of the manuscript taken from a region of a diameter of 600 nm polycrystalline 1T'-MoTe₂ is well labeled with the crystallographic planes of the 1T'-MoTe₂ structure, as shown in Figure S3, and the corresponding radii of the diffraction rings are listed in Table S1. The angular deviation of all the planes off the [001] zone-axis is within 5° indicating that the 1T' polycrystalline MoTe₂ film is textured along the [001] direction.

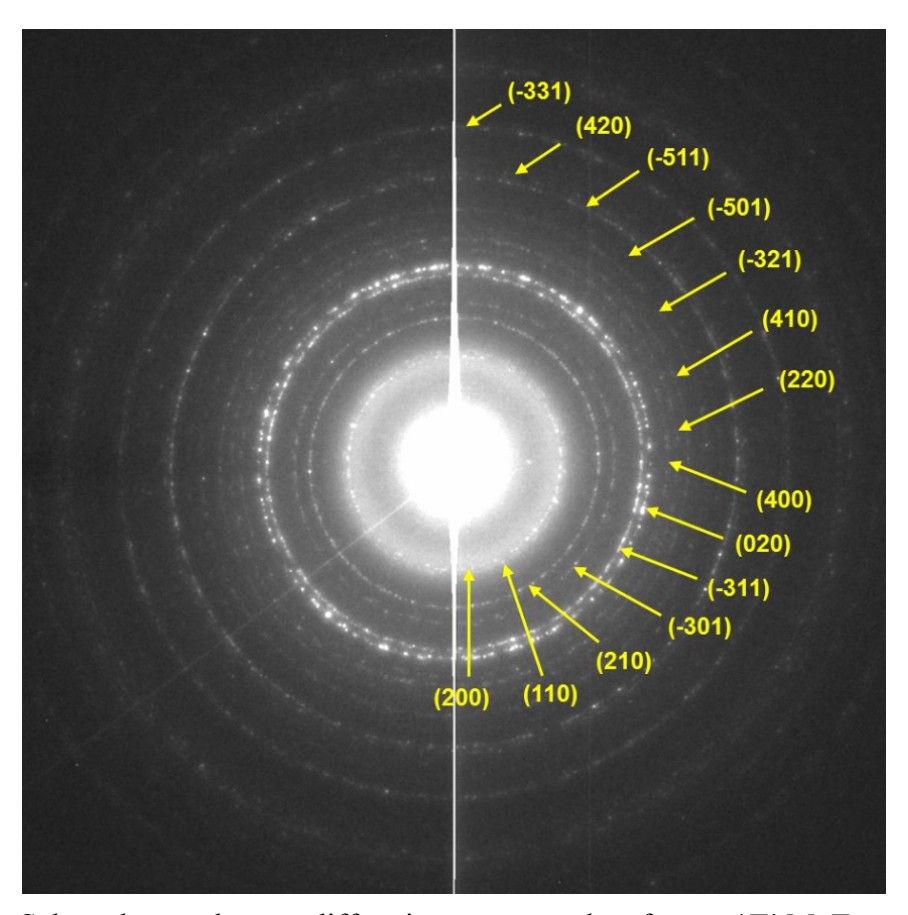


Figure S3. Selected-area electron diffraction patterns taken from a 1T'-MoTe₂ region with a diameter of 600 nm showing the polycrystalline diffraction rings. All the rings can be indexed as hk0 crystallographic planes (parallel to [001] zone-axis) or hkl crystallographic planes within a 5° off the [001] zone-axis, which suggests the 1T' polycrystalline film was textured along the [001] direction.

Table S1. Experimental and theoretical radiuses of diffraction rings of 1T' MoTe₂

| Experimental radius of diffraction ring (1/nm) | Theoretical radius of diffraction ring (1/nm) | | hkl ∩ (001) (degree) |
|--|---|------|-------------------------|
| 3.122 | 3.167 | 200 | 90 |
| 3.259 | 3.289 | 110 | 90 |
| 4.239 | 4.283 | 210 | 90 |
| 4.695 | 4.756 | -301 | 85.19 |
| 5.492 | 5.562 | -311 | 85.89 |
| 5.766 | 5.765 | 020 | 90 |
| 6.290 | 6.334 | 400 | 90 |
| 6.541 | 6.578 | 220 | 90 |
| 6.883 | 6.959 | 410 | 90 |
| 7.452 | 7.474 | -321 | 86.94 |
| 7.817 | 7.901 | -501 | 88.68 |
| 8.341 | 8.410 | -511 | 88.76 |
| 8.501 | 8.565 | 420 | 90 |
| 9.868 | 9.870 | -331 | 87.69 |

4. TEM/STEM of the thickness variation and misorientation in the 2H region:

Figure S4a is a dark-field (DF) TEM image taken from a round 2H region using a single (100) reflection as shown in Figure 2b. There are some small areas presenting a much darker contrast than the surrounding. Selected area electron diffraction pattern (SAEDPs) from the dark region SA-2 shows a very similar 2H pattern as the one from the large area SA-1 (Figures S4b and S4c). Figures S4d-S4g show the atomic models and the corresponding simulated diffraction patterns of 2H and 3R structures. It should be noted that the mixture of 2H and 3R stackings can have a similar diffraction pattern as that of 2H, and the DF image using (100) reflection can make the mixture region darker than the pure 2H region, assuming a flat film with a uniform thickness. However, the mixture region of 2H and 3R structures can be easily differenctiated from 2H by atomic resolution HRSTEM imaging, and we have never observed such a mixture in our film. The darker region in the DF images should be attributed to a smaller thickness in local area.

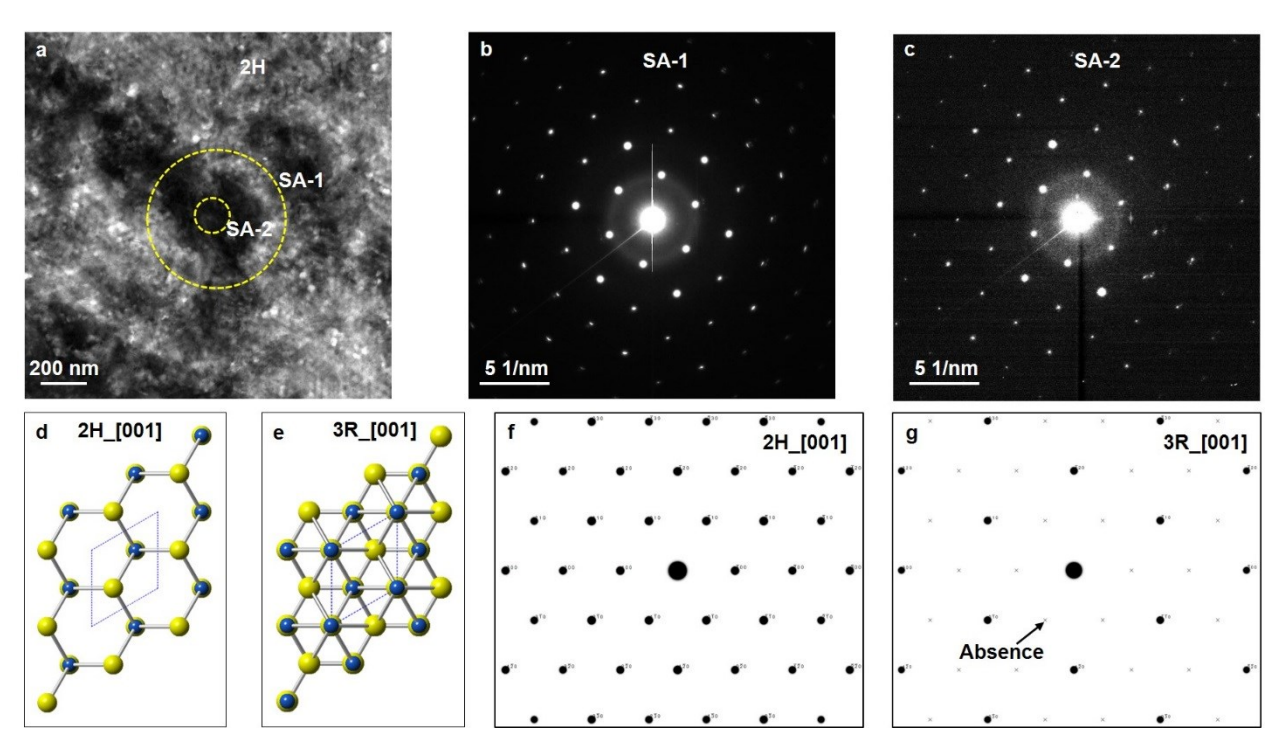


Figure S4. (a) Dark field TEM image taken from a round 2H region using a single (100) reflection. (b)-(c) Electron diffraction patterns taken from the selected areas of SA-1 and SA-2 shown in (a), respectively. (d)-(e) Atomic models of 2H and 3R structures, and (f)-(g) their corresponding simulated electron diffraction patterns.

Figure S5a shows an enlarged HRSTEM image of Figure 3e. The apparent downtrend of the intensity profile from A→B suggests a decreasing thickness in this region (Figure S5b). Figures S5c-S5e show the zoom-in images of the selected areas SA-1, SA-2 and SA-3 shown in Figure S5a, as well as their corresponding FFTs, evidencing the local misorientation in SA-2.

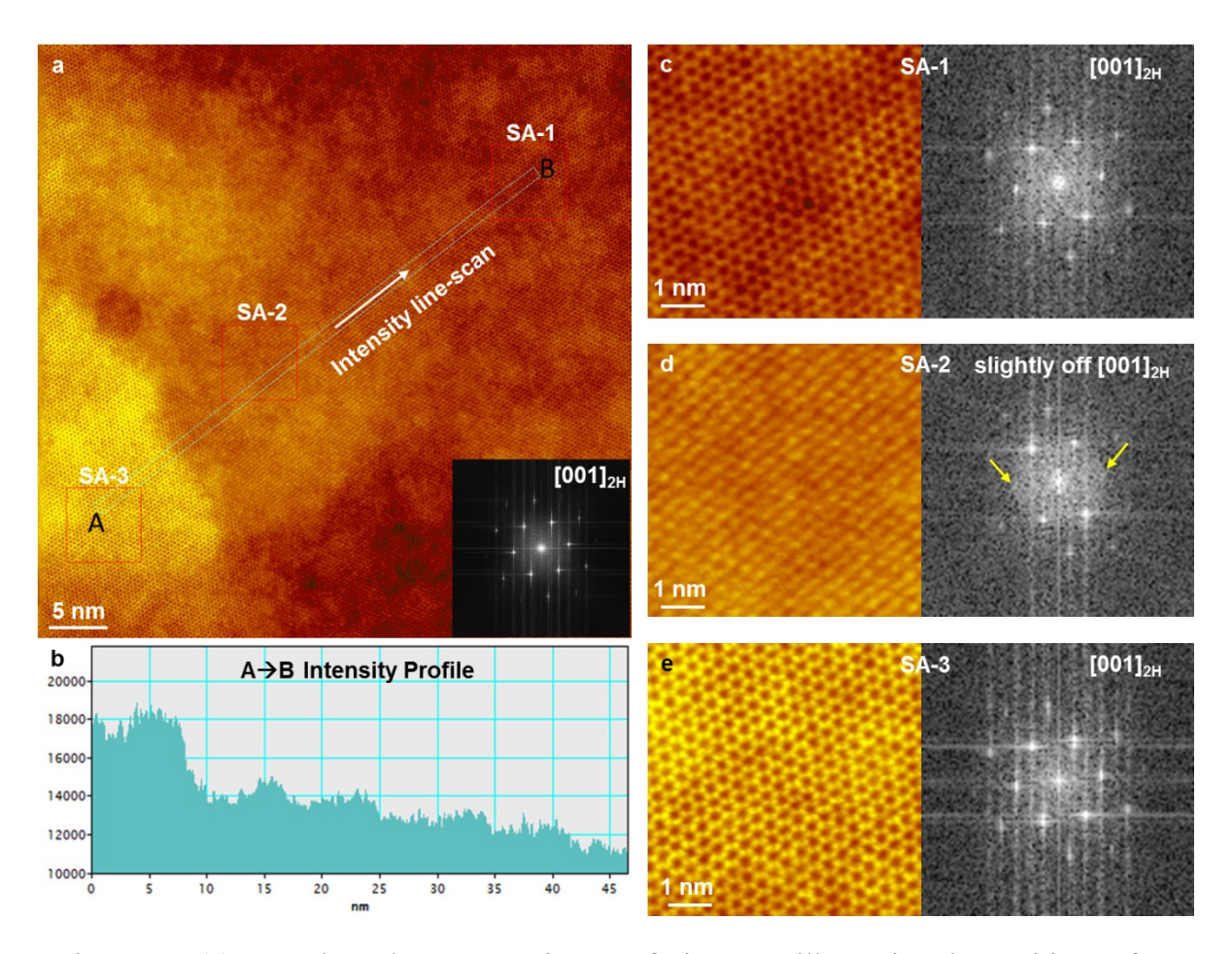


Figure S5. (a) An enlarged HRSTEM image of Figure 3e illustrating the positions of an intensity line-scan $A \rightarrow B$, and three selected areas for FFT. (b) Intensity profile showing the thickness variaton from $A \rightarrow B$. (c)-(e) The zoom-in images of the selected areas and their corresponding FFTs showing the local misorientation in SA-2.

5. Field-effect hole mobility at different temperatures:

We extracted the field-effect hole mobility, μ , from the temperature-dependent transfer characteristics for the 2H-only and 2H/1T' devices. The value of μ at a given temperature and $V_{\rm DS}$ is extracted at the maximum transconductance, g_m , which is defined as the maximum point in the derivative of the $I_{\rm D}$ vs. $V_{\rm GS}$ curve. The mobility is then calculated by

$$\mu = g_m \cdot L / (W \cdot C_{ox} \cdot V_{DS})$$
,

where L and W are the length and width of the device, respectively. $C_{\rm ox}$ is the gate dielectric capacitance and $V_{\rm DS}$ is the drain-to-source voltage. The extracted μ as a function of temperature for the 2H-only and the 2H/1T' devices are shown in Figure S6a and S6b, respectively.

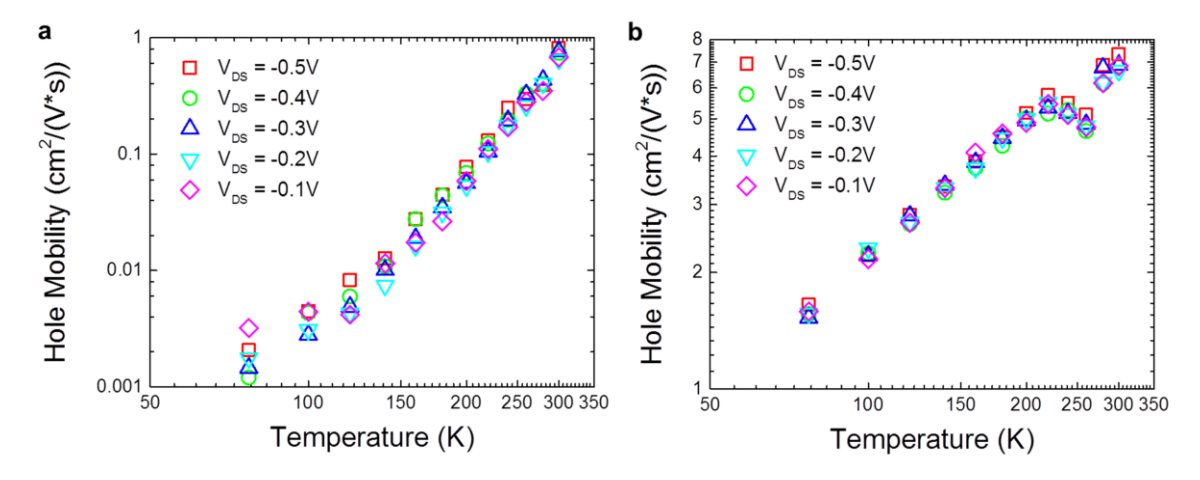


Figure S6. Field-effect hole mobility (log scale) as a function of temperature (log scale) for (a) the 2H-only device and (b) the 2H/1T' device in Figure 5 at different values of $V_{\rm DS}$. For the 2H/1T' device, the average length of the 2H region between the 1T' ends is used to calculate the mobility.

The 2H/1T' device shows about 10 times higher field-effect hole mobility than that of the 2H-only device because of the reduced contact resistances at the 1T'/metal and 2H/1T' interfaces. The mobility is relatively low because of the high defect density in the material. The 2H-only and 2H/1T' device show a power-law mobility vs. temperature dependence, $\mu \propto T^x$, where x = 5.9 and x = 1.3, respectively. The slope of the 2H/1T' device is close to the typical factor, x = 1.5, for Coulomb scattering dominant transport in the material due to the negligible effect from the contacts, which confirms the Ohmic nature of the metal/1T' and 2H/1T' interfaces. Coloumb-scattering-limited (rather than phonon-limited) mobility is not surprising in this material, give the rather high interface trap density in our samples. In addition, the dependence of $V_{\rm DS}$ on the mobility in the 2H/1T' device is less than that in the 2H-only device, which again confirms the Ohmic-like contacts in the 2H/1T' device. However, for the 2H-only device, the contact resistance and the sheet resistance are on the same order of magnitude, so we would expect higher $V_{\rm DS}$ dependence.

6. Temperature-dependent device behavior for another set of 2H-only and 2H/1T' devices:

Figure S7 shows the temperature-dependent transport characteristics of another set of 2H-only and 2H/1T' device from Sample 1, same substrate as the set used in Figure 5. The observed behavior is consistent with the results in Figure 5.

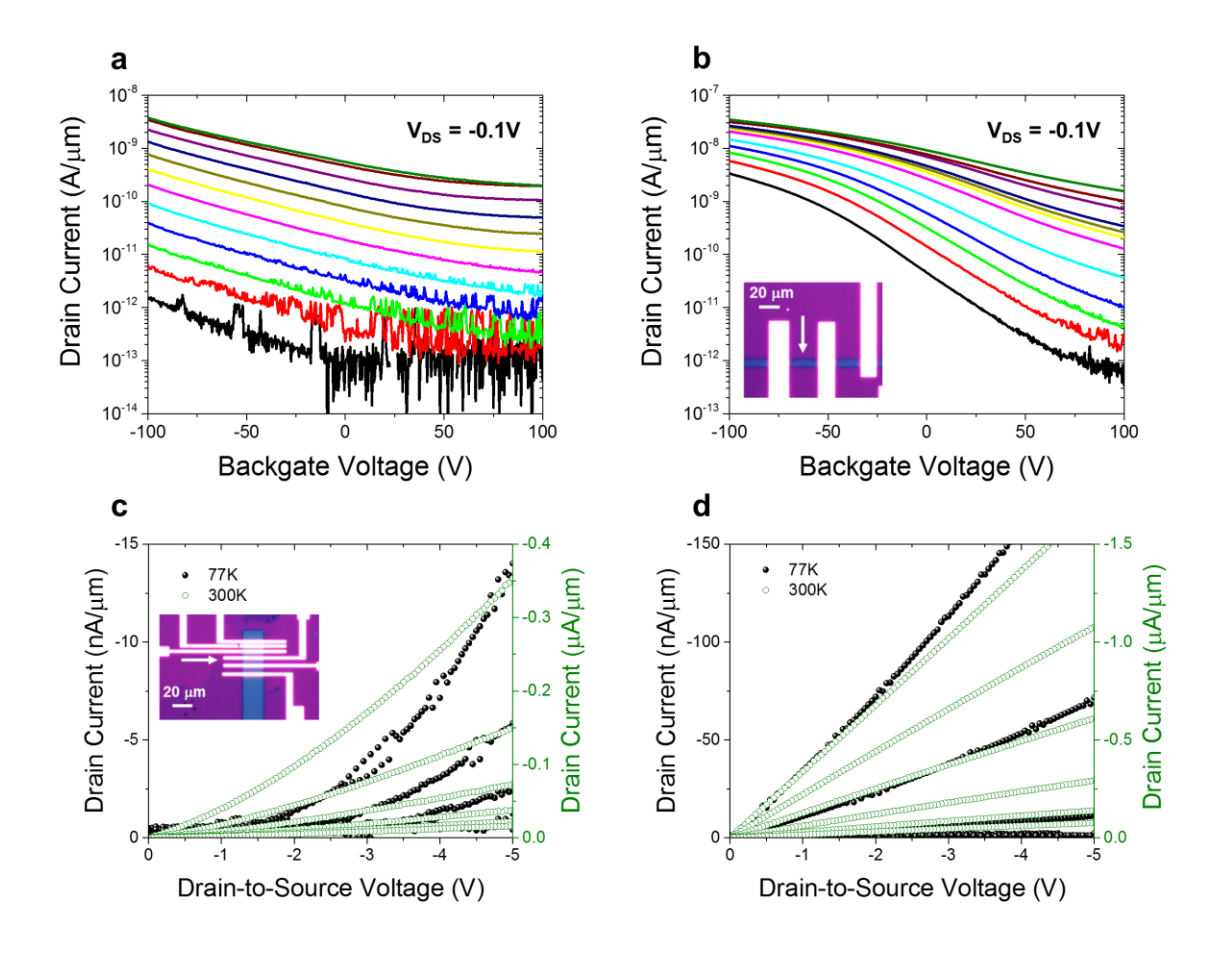


Figure S7. Temperature-dependent transport characteristics of another set of 2H-only and 2H/1T' device from the same growth as the set shown in Figure 5. (a)-(b) Transfer characteristics ($I_{\rm D}$ vs. $V_{\rm BG}$) of (a) 2H-only device and (b) 2H/1T' device at $V_{\rm DS}$ = -0.1 V for temperatures of 77 K (black curve), and from 100 K (red curve) to 300 K (olive curve), in steps of 20 K. (c)-(d) Output characteristics ($I_{\rm D}$ vs. $V_{\rm DS}$) of 2H-only and 2H/1T' device for $V_{\rm BG}$ varying from -100 V (top curve) to +100 V (bottom curve) in steps of +40 V at T = 77 K (black points) and T = 300 K (olive points). Optical images of the 2H-only and 2H/1T' device are shown as an inset in (c) and (b), respectively. The dimensions of the 2H-only device are $L_{\rm DS}$ = 4 μ m and W = 21 μ m, while the 2H/1T' device has $L_{\rm DS}$ = 26 μ m and W = 9 μ m (the length of the 2H region is about 20 μ m).

7. Device performance statistics:

To show the reproducibility of the devices from growth to growth, we plot histograms of normalized on resistances for devices fabricated on films from four different growths, as listed in Table S2. The film thickness of sample 1 is around 6 nm and the film thicknesses of sample 2-4 are around 10 nm.

Table S2. Number of devices of each type on samples from different growths

| Sample Index | Substrate Oxide Thickness | No. of 2H-only Devices | No. of 2H/1T' Devices | No. of 1T'-only Devices |
|--------------|------------------------------|---------------------------|--------------------------|----------------------------|
| 1 | 300 nm | 10 | 14 | 11 |
| 2 | 300 nm | 11 | 14 | 0 |
| 3 | 110 nm | 6 | 10 | 2 |
| 4 | 110 nm | 6 | 11 | 4 |

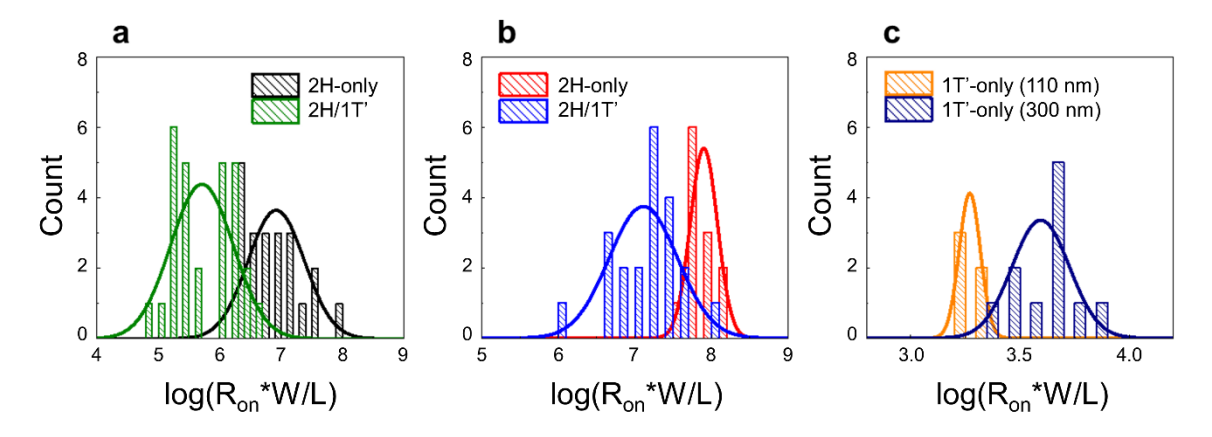


Figure S8. Histograms of normalized on resistances, $R_{\rm on}$, in log scale for (a) 2H-only and 2H/1T' devices made on 300 nm SiO₂/Si substrates at $V_{\rm BG}$ = -100 V and $V_{\rm DS}$ = -0.1 V, and (b) 2H-only and 2H/1T' devices made on 110 nm SiO₂/Si substrates at $V_{\rm BG}$ = -50 V and $V_{\rm DS}$ = -0.05 V, with a bin size of 0.2, and (c) 1T'-only devices on 300 nm and 110 nm SiO₂/Si substrates at $V_{\rm BG}$ = 0 V and $V_{\rm DS}$ = -0.05 V, with a bin size of 0.1. The 2H-only and 2H/1T' devices in each histogram come from two different samples, and the 1T'-only devices come from three different samples. All on resistances are multiplied by the channel length, L, and divided by the channel width, W. In (a), the distribution of the 2H-only devices (2H/1T' devices) has a mean of 6.92 (5.71) and standard deviation of 0.46 (0.5). In (b), the distribution of the 2H-only devices (2H/1T' devices) has a mean of 7.9 (7.11) and standard deviation of 0.18 (0.45). In (c), the distribution of the 1T'-only devices on the 110 nm (300 nm) SiO₂/Si substrate has a mean of 3.27 (3.59) and standard deviation of 0.05 (0.13).

Histograms of normalized on resistances for 2H-only and 2H/1T' devices fabricated on 300 nm SiO₂/Si substrates (Sample 1 and 2) and 110 nm SiO₂/Si substrates (Sample 3 and 4) are shown in Figures S8a and S8b, respectively. The on resistances of 2H-only and 2H/1T' devices were taken at $V_{\rm BG} = -100$ V and $V_{\rm DS} = -0.1$ V for Samples 1 and 2, and at $V_{\rm BG} = -50$ V and $V_{\rm DS} = -0.05$ V for Samples 3 and 4. Overall, 2H/1T' devices show lower on resistance than that of 2H-only devices owing to the reduced contact resistance at the metal/1T' interface, in consistent with the results in the manuscript. Figures S8c shows histograms of normalized on resistance of 1T'-only devices fabricated on two different substrates at $V_{\rm BG} = 0$ V and $V_{\rm DS} = -0.05$ V. It should be noted that the normalized on resistance levels for the same type of devices from two substrates do not match well because of different bias conditions, dielectric thicknesses, and film thicknesses.

8. Effective Schottky barrier height extraction:

The slopes of the Arrhenius curves are $(qV_{DS}/\eta - \Phi_{SB})$, so the effective Schottky barrier height, Φ_{SB} , can be extracted by plotting the slopes vs. V_{DS} and then extrapolating to $V_{DS} = 0$. A representative plot of the extraction for a 2H-only device at a given V_{BG} is shown in Figure S9. Φ_{SB} is extracted for all values of V_{BG} .

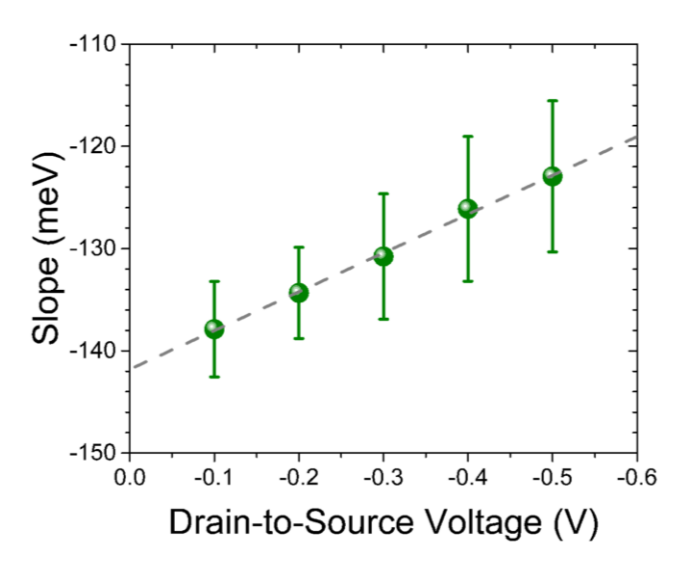


Figure S9. Slope of the Arrhenius plot for the same 2H-only device in Figure 5 of the manuscript plotted $vs.\ V_{DS}$ at $V_{BG} = 0V$.

9. Comparison of $V_{\rm BG}$ -dependent effective Schottky barrier heights for different devices;

Figure S10 compares the $V_{\rm BG}$ -dependent effective Schottky barrier heights for devices in Figure 5 and devices in Figure S7. The overall values of the barrier heights and the gate-bias dependence are in excellent agreement with each other.

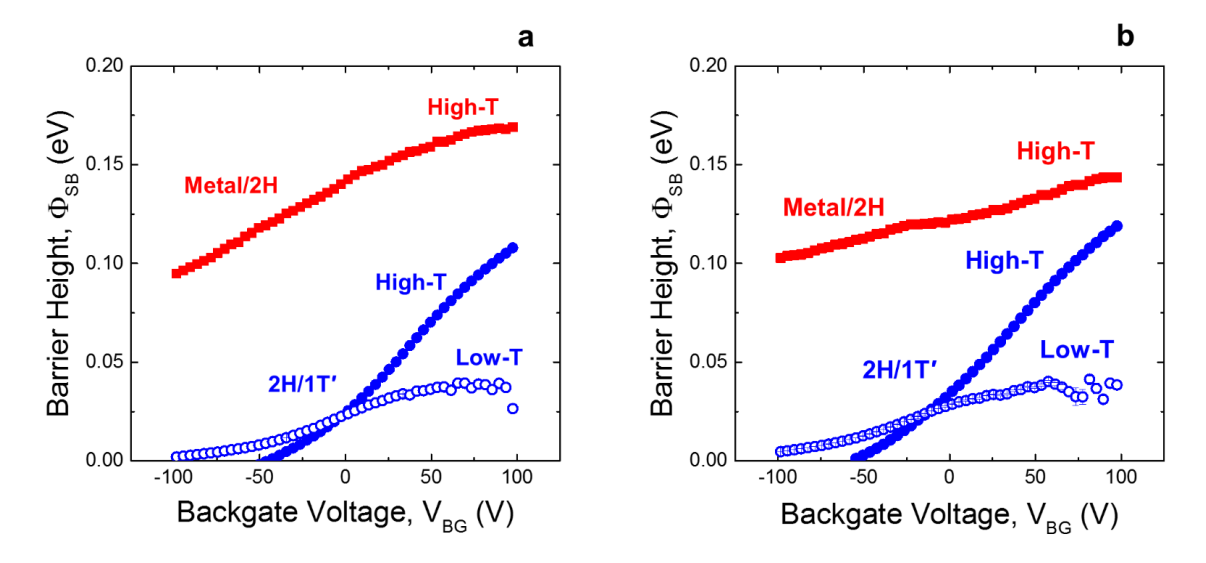


Figure S10. (a) Effective Schottky barrier height of the 2H-only device (shown in Figure 5) in the high temperature regime (red squares) and 2H/1T' device (shown in Figure 5) in the high- (close blue circles) and low- (open blue circles) temperature regimes as a function of $V_{\rm BG}$. (b) Effective Schottky barrier height of the 2H-only and 2H/1T' devices shown in Figure S7 as a function of $V_{\rm BG}$.

10. Effective Schottky barrier height statistics:

To further show that the observed large energy barrier difference at the metal/2H and 2H/1T' interface is not particular to the devices shown in the manuscript, the effective energy barrier heights at $V_{\rm BG} = 0$ for several 2H-only and 2H/1T' devices were extracted and summaried in the box plots shown in Figure S11. The channel thicknesses of these devices range from 6 nm to 10 nm. The two box plots are relatively short suggesting that the overall barriers at each interface have a high level of agreement. The barrier heights at the metal/2H interfaces are consistently ~100 meV higher than for the 2H/1T' interfaces.

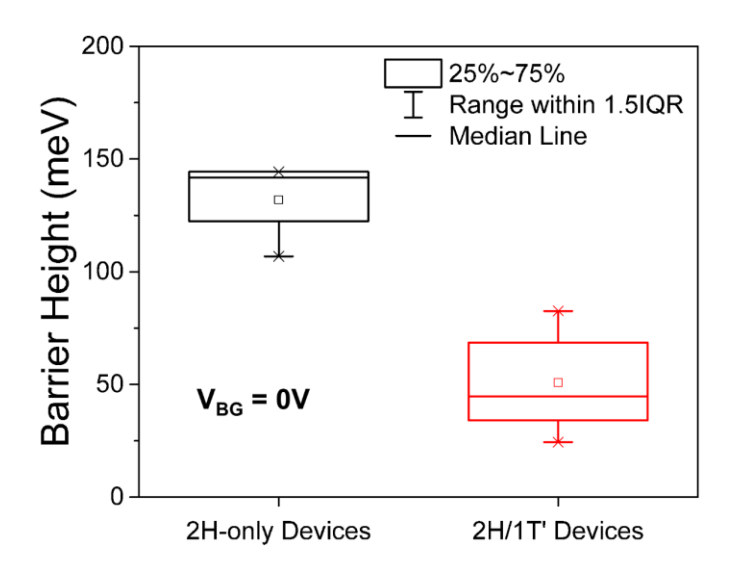


Figure S11. Box plots for effective Schottky barrier heights at $V_{\rm BG} = 0$ for five 2H-only and five 2H/1T' devices. The 25th~75th percentiles are shown as boxes, and ranges within 1.5 interquartile range (IQR) are shown as whiskers. The mean (median) are 132 meV (142 meV) for 2H-only devices and 51 meV (45 meV) for 2H/1T' devices.

11. Flat-band barrier extraction at the 2H/1T' interface:

The effective energy barrier height as a function of the back-gate voltage is plotted in Figure S12 for the 2H/1T' device from Figure 5 in the high-temperature regime. The flat-band barrier height, Φ_{SB0} , which is the barrier at $V_{BG} = V_{FB}$ (flat-band voltage), is extracted at the point where the slope deviates the linear dependence on V_{BG} . As illustrated in Figure S12, the Φ_{SB0} for the 2H/1T' device is estimated to be between 20 meV (at $V_{BG} = -6.5$ V) and 40 meV (at $V_{BG} = 19.5$ V). Since there is no thermally-activated energy barrier at the metal/1T' MoTe₂ interface, this extarcted barrier is at the 2H/1T' interface.

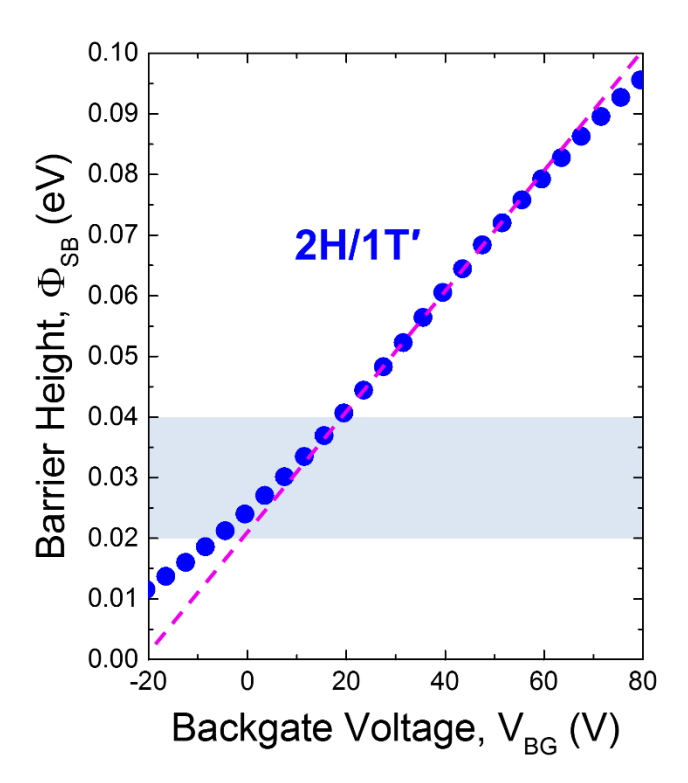


Figure S12. Effective Schottky barrier height of the 2H/1T' device in the high temperature regime as a function of V_{BG} . The dash magenta line fits the linear portion of the curve, and the flat-band barrier height is estimated to be between $\sim 30 \pm 10$ meV.

12. Band diagrams for the metal/2H and 2H/1T' interfaces under different bias conditions:

Figure S13a shows the Φ_{SB} vs. V_{BG} plot for the metal/2H and 2H/1T' devices from Figure 5 in the high-temperature regime, where Figures S13b and S13c show schematic illustrations of the lateral energy band diagrams. The diagram in Figure S13b shows that the weaker backgate voltage dependence is due to the relatively long transfer length under the contact metal, as opposed to at the edge of the contact as in the case of the 2H/1T' devices (Figure S13c).

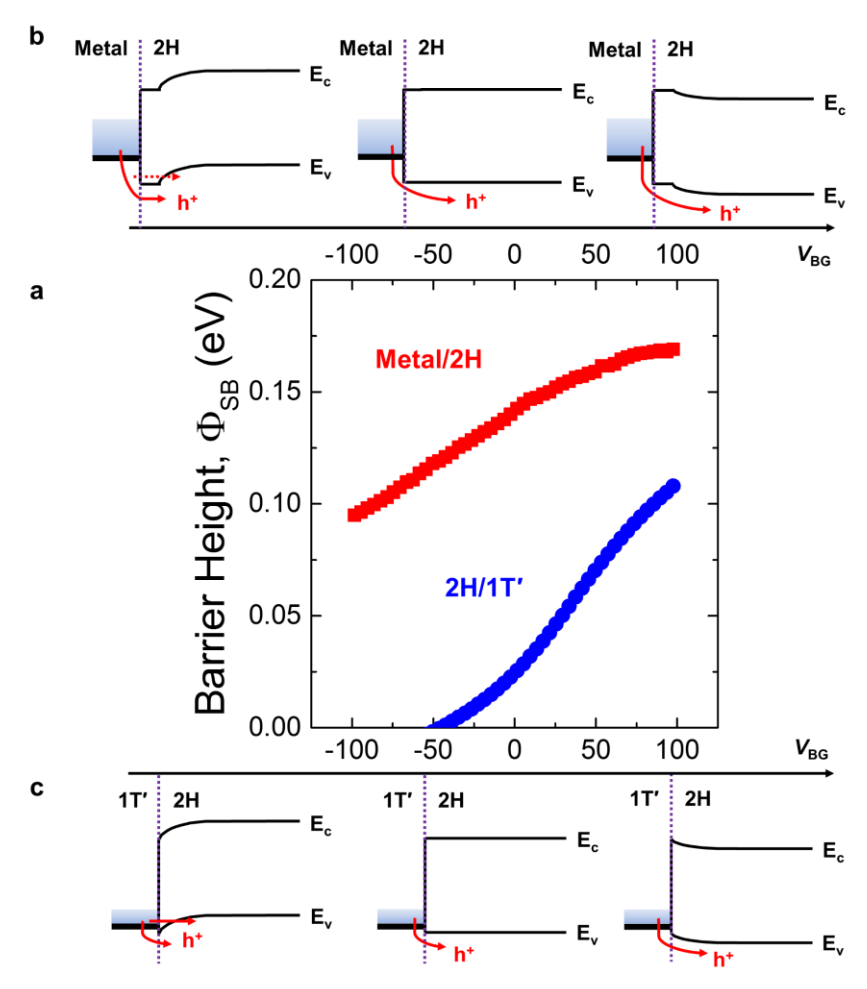


Figure S13. Band diagrams for the 2H-only and the 2H/1T' device under different values of backgate voltage, $V_{\rm BG}$. (a) Effective Schottky barrier height of the 2H-only device (red squares) and 2H/1T' device (close blue circles) as a function of $V_{\rm BG}$. (b)-(c) The gate voltage modulations of the band diagrams and hole (h⁺) injections at the (b) metal/2H interface and (c) 2H/1T' interface when $V_{\rm BG}$ increases from -100 V to +100 V. The purple dotted lines indicate the metal/2H and 2H/1T' interfaces, respectively. In (b), the pinned regions underneath the metal contacts inhibits the gate modulation of the effective barrier height, $\Phi_{\rm SB}$, while in (c) the lateral nature of the interface allows stronger modulation of $\Phi_{\rm SB}$.

13. Band structures of 2H and 1T' MoTe2:

Figure S14a and S14b show the computed band structures of 5-layer 2H and 5-layer 1T' MoTe₂, respectively. Using PBE/GGA with spin-orbit coupling, the 5-layer 2H MoTe₂ is found to be semiconductor with an indirect band gap of 0.75 eV, which is smaller than the experimentally extracted value because it is well known that DFT simulation underestimates the

band gap. For the 5-layer 1T' MoTe₂, the band gap is closed and the conduction band minimum (CBM) and the valance band maximum (VBM) are overlapped. The states of the conduction band and the valance band are not separated completely; therefore the 5-layer MoTe₂ is semimetallic.

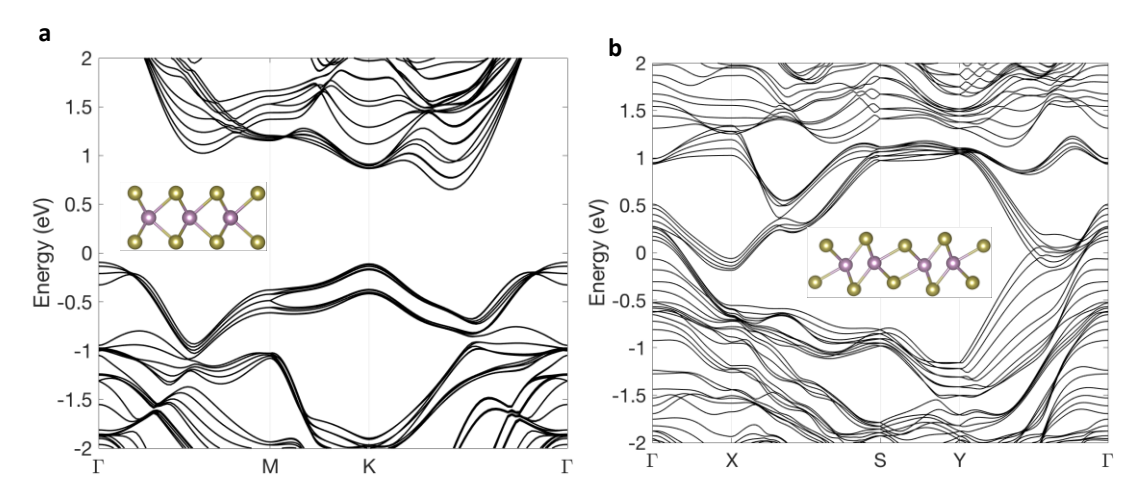


Figure S14. (a)-(b) Band structure of 5-layer 2H and 5-layer 1T' MoTe₂, respectively. Spin orbital coupling is included. The insets are the unit cells. (The insets are side views of the atomic structure for 1-layer system.) The Fermi level is set at zero energy.

14. Band gap of 2H MoTe₂ and barrier height at the 2H/1T' interface vs. number of layers:

The thickness-dependent band gap calculated by taking the difference between CBM and VBM is shown in Figure S15a. The barrier heights (for holes) at the 2H/1T' interface were calculated based on the Schottky-Mott (SM) model, S1 which assumes that the barrier for holes is the energy difference between the work function of the metal and the VBM at the semiconductor. The calculated barrier heights as a function of the number of layers are shown in Figure S15b. The calculated barrier height for 5-layer 2H/1T' interface is about 77 meV, which is on the same order as the electrically extracted value from Figure 7 in the manuscript. However, is has been demonstrated that the SM model is insufficient in predicting the precise barrier height at the interface of 2D lateral heterostructures. S2 Therefore, more sophisticated models are needed to estimate the barriers more accurately, such as computing the lateral heterostructures by constructing a supercell which consists of both phases.

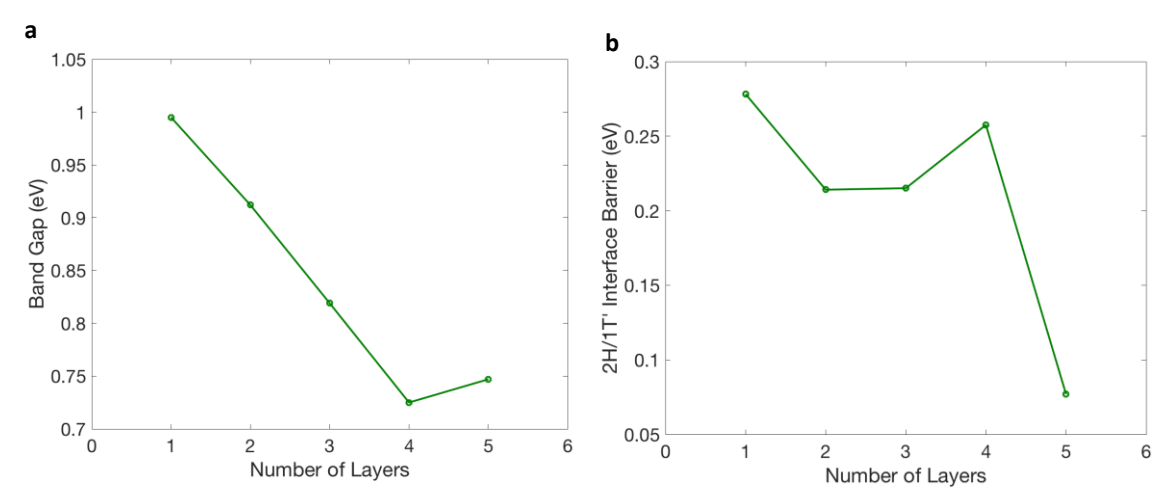


Figure S15. (a) Calculated band gap of 2H-MoTe₂, and (b) calculated barrier height at the 2H/1T' interface as a function of the number of layers in the MoTe₂.

Supplementary References

- S1 Mott, N. F. The Theory of Crystal Rectifiers. *Proc. R. Soc. London, Ser. A* **1939**, *171*, 27-38.
- S2 Zhang, J.; Xie, W.; Zhao, J.; Zhang, S. Band Alignment of Two-Dimensional Lateral Heterostructures. *2D Mater.* **2017**, *4*, 015038.